



Technische Universität München Fakultät für Physik

## **Dissertation**

Bottom-up Construction and Characterization  
of Low-dimensional Graphene- and  
Phthalocyanine-based Nanostructures

**Wei Ran**





Technische Universität München Fakultät für Physik

Lehrstuhl E20 – Molekulare Nanowissenschaft an Grenzflächen

# Bottom-up Construction and Characterization of Low-dimensional Graphene- and Phthalocyanine-based Nanostructures

**Wei Ran**

Vollständiger Abdruck der von der Fakultät für Physik der Technischen Universität München zur Erlangung des akademischen Grades eines Doktors der Naturwissenschaften (Dr. rer. nat.) genehmigten Dissertation.

Vorsitzender: apl. Prof. Dr. Norbert Kaiser

Prüfer der Dissertation: 1. Prof. Dr. Johannes Barth

2. Priv.-Doz. Dr. Markus Lackinger

Die Dissertation wurde am 13.10.2021 bei der Technischen Universität München eingereicht und durch die Fakultät für Physik am 14.11.2021 angenommen.



## Abstract

Bottom-up self-assembly using distinct intermolecular interactions of tailor-made tectones is a promising way for building atomically-precise nano-architectures. Nanostructures stabilized by covalent or metal-coordination bonds can exhibit a very high stability. Scanning tunneling microscopy (STM) is utilized for the characterization of their structures. Here, we present a combined study using scanning tunnelling microscopy and an in-house developed electrospray-controlled ion beam deposition system under ultra-high vacuum to explore the deposition, the assembly as well as chemical reactions of graphene nanoribbons (GNRs) and  $\text{PcZn(OH)}_8$  on the close-packed Ag(111) surface. In my thesis, a systematic investigation of the self-assembly and polymerization of N-doped atomically-precise and homogenous graphene nanoribbons, synthesized in solution, on the close-packed, atomically flat silver surface was conducted. By employing thermal activation at different temperatures, we achieved an on-surface polymerization through organo-Ag bonds. Via a statistical analysis of the distances between neighboring bright protrusions, we can conclude that the observed polymeric chains are stabilized by Ag- organometallic bridges. Additionally, the self-assembly of  $\text{PcZn(OH)}_8$  molecules on silver, as well as their coordination with Fe adatoms was investigated. STM provides the atomic resolution topography of the architecture revealing novel coordination motifs with metal atoms on Ag (111). As a step towards the realization of micro-devices based on GNRs, the fabrication and characterization of test-device based on 6-CGNR-I and 6-CGNR-II on a diamond surface was investigated. Using prototype devices, we characterized the electronic properties of the GNRs. With the on-surface synthesis of graphene-based nanostructures we introduce a novel way to polymerize GNRs and open up new pathways for applications in nanoelectronics technologies of the future.

## Zusammenfassung

Die Selbstorganisation von maßgeschneiderten molekularen Bausteinen durch intermolekulare Wechselwirkungen ist ein vielversprechender Weg zum Aufbau von Nanoarchitekturen mit atomarer Präzision. Nanostrukturen mit kovalenten oder Metall-Koordinationsbindungen können eine sehr hohe Stabilität aufweisen. Um ihre Strukturen zu untersuchen wird die Rastertunnelmikroskopie eingesetzt. Hier stellen wir eine kombinierte Studie vor, bei der wir die Rastertunnelmikroskopie und ein selbst entwickeltes elektro spray Ionenstrahldepositionssystem im Ultrahochvakuum nutzen, um die Abscheidung, die Anordnung sowie die chemischen Reaktionen von Graphen-Nanobändern (GNRs) und  $\text{PcZn(OH)}_8$  auf atomar wohldefinierten Edelmetalloberflächen zu untersuchen. In der vorliegenden Dissertation wurde eine systematische Untersuchung der Selbstorganisation und Polymerisation von N-dotierten atomar präzisen und homogenen Graphen-Nanobändern, die in Lösung synthetisiert wurden, auf dicht gepackten, atomar flachen Silberoberflächen durchgeführt. Bei thermische Aktivierung beobachten wir eine Polymerisation der GNRs auf der Oberfläche durch Bildung von Organo-Ag-Bindungen. Über eine statistische Analyse der Abstände zwischen benachbarten Molekülen können wir darauf schließen, dass die beobachteten Polymerketten durch Ag-koordinierte Brücken stabilisiert werden. Darüber hinaus wurde die Selbstorganisation von  $\text{PcZn(OH)}_8$ -Molekülen auf Silber sowie ihre Koordinierung mit Fe-Atomen untersucht. STM ermöglicht Einblicke in die Topologie mit atomarer Auflösung und zeigt neuartige Koordinationsmotive mit Metallatomen auf Ag(111). Als ein Schritt in Richtung der Erzeugung von Mikrobauteilen auf der Basis von GNRs wurde die Herstellung von Testbauteilen mittels 6-CGNR-I und 6-CGNR-II auf einer Diamantoberfläche untersucht und außerdem die elektronischen Eigenschaften der GNRs charakterisiert. Mit der Erforschung der Synthese von Graphen-basierten Nanostrukturen auf Oberflächen stellen wir neue Wege für deren Anwendung in der Nanoelektronik der Zukunft zur Verfügung.

# Contents

1. Introduction .....	1
2. Experimental methods: theory and setup .....	5
2.1 Scanning tunnelling microscopy .....	5
2.1.1 The tunnelling effect.....	5
2.1.2 Scanning modes .....	9
2.1.3 Experimental setup .....	10
2.2 Electro spray-controlled ion beam deposition.....	13
2.2.1 Electro spray ionization (ESI) .....	14
2.2.2 Overview over the combined ES-CIDB and VT-STM setup .....	15
3. Results and discussions.....	18
3.1 Depositing Molecular Graphene Nanoribbons on Ag(111) by Electro spray Controlled Ion Beam Deposition: Self-assembly and On-Surface Transformations .....	18
3.1.1 Introduction .....	18
3.1.2 Sample Preparation.....	20
3.1.3 Coverage-dependent self-assembly .....	22
3.1.4 Chemical reactivity of NR10 on Ag(111) .....	25
3.1.5 Summary and conclusion.....	32
3.2 $\text{PcZn(OH)}_8$ on Ag(111) .....	34
3.2.1 Introduction .....	34
3.2.2 On-surface synthesis procedure.....	36

3.2.3	The self-assembly and metal adatom coordination of $\text{PcZn(OH)}_8$ on $\text{Ag(111)}$ ....	38
3.2.4	Summary and conclusions .....	45
3.3	The fabrication of microdevices based on GNRs .....	46
3.3.1	Introduction .....	46
3.3.2	Sample Preparation.....	49
3.3.3	Results and discussion .....	55
3.3.4	Summary and conclusion.....	58
4.	Conclusions.....	59
5.	Acknowledgements.....	61
	References.....	62

# 1. Introduction

In 1959, a concept “There’s Plenty of Room at the Bottom” was proposed by Richard Feynman in his famous talk,<sup>1</sup> while Norio Taniguchi subsequently proposed a concept to process and manipulate materials on the atomic or single-molecular level 1974.<sup>2</sup> Since then, research in nanotechnology attracted widespread attention in science, with emphasis in the controlled construction of nanostructures. Thus techniques capable of producing features in the range below 100 nanometers were developed and applied. Molecular beam epitaxy (MBE), a technique which can be used to fabricate thin-films in ultra-high vacuum (UHV) was invented in 1968<sup>3</sup> and played an important role in the development of nanoscience.<sup>4</sup> Atomic layer deposition (ALD), a complementary method in the synthesis of nanomaterials, was introduced by Thumo Suntola.<sup>5</sup> In 1981, scanning tunneling microscopy (STM) was invented by Binnig and Rohrer in the IBM Rüschlikon laboratory. It could be used to both observe and manipulate structures on surfaces at the atomic scale. Its theoretical basis is the quantum tunneling effect: electrons can transfer through a non-contact gap between two conductors (or semiconductors). Subsequently, in 1986, atomic force microscopy (AFM) was invented. In the past decades, nanotechnology developed in a rapid way. A multitude of nanomaterials with different novelties have been developed and explored.

To fabricate nanoarchitectures, there are two different approaches: “top-down” and “bottom-up”. Within the top-down approach, some novel methods attract a lot of interest such as microcontact printing,<sup>6-9</sup> inkjet printing,<sup>10</sup> “Dip-Pen” nanolithography.<sup>11-13</sup> Classical optical lithography techniques are widely used in semiconductor industry. By using that method, the central processing units (CPUs), the core technology of billions of computers, cellphones and other digital devices techniques, are produced. To fabricate CPUs, large silicon wafers are cut into smaller pieces and processed by sophisticated lithography techniques. Moore’s Law indicates that the number of transistors on an integrated circuit will double every 24 months.<sup>14</sup> Following this prediction, silicon based nanolithography will quickly enter the atomistic domain and thus may reach fundamental limits. Therefore, scientists explore other methods to achieve further miniaturization. Opposite to the top-down method is the bottom-up approach, which is based on the manipulation of single molecules or atoms to build desired nanostructures through e.g. the self-assembly of molecules with specific functional groups. In “bottom-up” strategies, the atoms and molecules could be manipulated to fabricate electronics and machines

## 1. Introduction

at the nanoscale. Surface chemistry brings a novel effective way of bottom-up fabrication of artificial construction of nanostructures. It focuses on chemical systems comprising assembled molecular building blocks, which can either be put together to form the desired structure by specialized instruments, step-by-step, or at a more advanced level, may assemble themselves automatically, interacting with each other through forces of varying strength and range, such as hydrogen bonds,<sup>15–18</sup> metal-organic coordination,<sup>19</sup>  $\pi$ - $\pi$  stacking,<sup>20</sup> dipole interactions, van der Waals interactions<sup>21</sup> etc. A lot of research focused on supramolecular chemistry on surfaces has a potential use in many fields, such as catalysis, biosensors, data storage, nanomachines.<sup>22–25</sup>

Recently, research on covalently linked nanoarchitectures has attracted a lot of attention,<sup>26–31</sup> since they have a higher thermal, mechanical, and chemical stability. Until now, a large amount of covalent bond forming reactions occurring on surfaces have been explored, including Schiff base formation,<sup>32–36</sup> Ullmann coupling,<sup>26,37–42</sup> and others. For the fabrication of the desired nanoarchitectures using complex molecules on metals, the investigations of adsorption geometry, mobility and lateral intermolecular interactions are very important. These are influenced by intermolecular interactions, the substrate environment, chemical nature and symmetry.<sup>43–45</sup> A current example of this approach can be found in the development of graphene nanoribbons doped with heteroatoms,<sup>46–50</sup> which has attracted a lot of attention, because their electronic structure can be tailored by the dopants.<sup>51</sup> The introduction of additional n-type carriers in carbon systems by N-doping could have potential applications for many fields, such as information processing devices, energy conversion and storage, as well as biosensing applications.<sup>52–57</sup> Nevertheless, it is still very challenging to control the length, width and homogeneity of GNRs (graphene nanoribbons) precisely and additional byproducts tend to be present on the surface (e.g. halogen atoms for Ullman coupled GNRs). Thus, a technique which could be used for the deposition of well-defined, defect-free GNRs on surfaces would be highly desirable. In chapter 3.1, we investigate the deposition of atomically-precise and homogenous GNRs on Ag (111) by an in-house developed electrospray-controlled ion beam deposition (ES-CIBD) system. The ES-CIBD is employed due to its capability to deposit ionized organic molecules, which are difficult to be deposited by using organic molecular beam epitaxy (OMBE) because of their thermal instability. STM measurements under UHV

conditions evidence that the deposited GNRs land intact on the Ag (111) surface (morphology of the molecules is preserved) without any contamination or additional species. One of the experimental tools we used is STM, which allows to obtain real-space imaging of a surface with submolecular resolution, the detailed molecular arrangement and even the orientation of the molecules on the surface. These two techniques are described with more details in chapter 2.

Metal-organic frameworks (MOFs) are crystalline porous materials, which can be obtained by combining organic linkers with metal containing nodes. In the recent decade, MOF based materials attracted growing interest in the field of both functional materials and inorganic chemistry, due to the tuneability of structures and functionalities on large surface areas and their ultrahigh porosity. 2D MOF nano-sheets can be used in many fields, including gas separation, energy conversion and storage, catalysis, sensing, etc. In chapter 3.2, a bottom-up approach was employed to investigate the formation of a single layer 2D-MOF. In this chapter,  $\text{PcZn(OH)}_8$  are deposited on an atomically flat Ag (111) surface by using ES-CIBD under UHV conditions. Fe atoms are added to this surface by atomic sublimation. STM images reveal that  $\text{PcZn(OH)}_8$  molecules can form variable self-assemblies on the substrate, depending on the surface stoichiometry of  $\text{PcZn(OH)}_8$ : Fe and the annealing treatment.

Because of their unique physical properties, research on GNRs is growing rapidly. GNRs can be applied in many fields, such as nano-electronic, spintronic, and optoelectronic devices. Band gaps introduced by quantum confinement and edge effects in narrow graphene ribbons make the GNRs outstanding materials to realize field-effect transistors. In order to fabricate GNRs, researchers have developed several approaches, including lithographic patterning, chemical synthesis, chemical sonication techniques etc. As we demonstrate in chapter 3.1, long chains of GNRs can be fabricated on metal substrates in UHV. Within this thesis, we employed two different structures of GNRs synthesized in solution (6-CGNR-I and 6-CGNR-II) and investigate them in chapter 3.3. These GNRs have an identical aromatic core but alkyl side chains at different peripheral positions. According to theoretical modeling, 6-CGNR-II with alkyl chains at the innermost positions has a lower optical and electronic bandgap than the planar 6-CGNR-I substituted at the outermost positions. According to the experimental results, based on UV-vis, near-infrared (NIR) absorption and photoluminescence excitation (PLE) spectroscopy, the theoretical prediction is correct. Furthermore, we fabricated model GNRs devices based on 6-CGNR-I and 6-CGNR-II by using optical lithography to investigate their

## ***1. Introduction***

characteristic transport behavior and explore the potential difference of resulting electrical properties.

Chapter 4 gives conclusions and an outlook regarding future perspectives.

## **2. Experimental methods: theory and setup**

The techniques and instrumentation used for the experiments in this thesis will be introduced here. The main methods are STM, ES-CIBD and photolithography.

### **2.1 Scanning tunnelling microscopy**

STM was invented by Binnig and Rohrer in 1983.<sup>58</sup> It can be employed to investigate surface properties with high precision. In the following, the fundamentals of scanning tunneling microscopy are described.

#### **2.1.1 The tunnelling effect**

The tunneling effect arises from quantum mechanics. In classical mechanics, a particle cannot overcome a potential barrier higher than its overall energy. However, in quantum mechanics, a particle can propagate through a potential barrier, even if its energy is smaller than the barrier potential. STM utilizes the tunneling of electrons.

## 2. Experimental methods: theory and setup

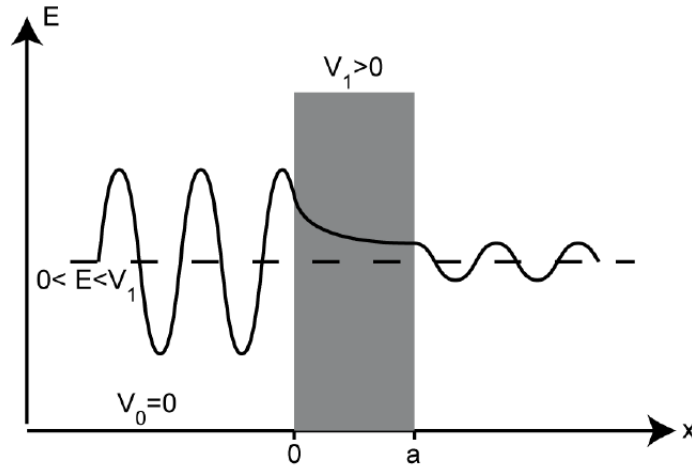


**Fig. 2.1:** Schematic illustration of quantum tunneling effect.<sup>59</sup>

In quantum mechanics an electron can be considered as a wave. In the one-dimensional case, its wave function  $\psi$  can be described by the time independent Schrödinger equation (TISE)

$$\frac{d^2\psi}{dx^2} = \frac{2m}{\hbar^2}(V_x - E)\psi \quad (2.1)$$

where  $m$  is the electron mass,  $E$  the energy of the electron,  $\hbar$  the reduced Plank constant,  $x$  the spatial coordinate and  $V$  the potential energy. Here we can consider a simple barrier with  $V = V_1 > E$  for  $0 \leq x \leq a$ , and  $V = V_0 = 0$  for  $x \leq 0$  and  $x \geq a$  (Fig. 2.1).

The solution for the TISE is:

$$\psi = \begin{cases} A_1 e^{ikx} + A_2 e^{-ikx}, & (x \leq 0) \\ B_1 e^{\kappa x} + B_2 e^{-\kappa x}, & (0 \leq x \leq a) \\ C_1 e^{ikx} + C_2 e^{-ikx}, & (x \geq a) \end{cases} \quad (2.2)$$

where  $A_1, A_2, B_1, B_2, C_1,$  and  $C_2$  are constants,  $k = \sqrt{\frac{2mE}{\hbar^2}}$  and  $\kappa = \sqrt{\frac{2m(V_1 - E)}{\hbar^2}}$ . When  $x \geq a$ , we can have waves passing through the potential barrier, with  $C_2$  being set to zero. After imposing the continuity of the wave function at 0 and  $a$ , the transmission coefficient can be described as:

$$T = \left(1 + \frac{(k^2 + \kappa^2)^2}{4k^2\kappa^2} \sin^2(\kappa a)\right)^{-1} \quad (2.3)$$

this can be written as:

$$T \approx \frac{16k^2\kappa^2}{(k^2+\kappa^2)^2} e^{-2\kappa a} \quad (2.4)$$

when considering a large attenuating barrier. The transmission coefficient is dependent on the tunneling barrier width exponentially. In this case, the tunneling current can be expressed as:

$$I_t = C e^{-2\kappa a} = C e^{-2\frac{\sqrt{2m(V_1-E)}}{\hbar}a} \quad (2.5)$$

where  $C$  is a constant.

This equation for the tunneling current describes an individual electron penetrating through a potential barrier. In case of tunneling between two metals, the tunneling current exponentially depends on the distance between them.

In a metal-vacuum-metal system (e.g. sample-vacuum-tip), the vacuum level of the metal corresponds to the potential barrier  $V_1$ . We assumed that the work functions of sample and tip are the same. Applying a voltage  $V_b$  between them, leads to a net tunneling current. Since electron conductivity is a must for detecting a tunneling current, STM cannot be used to investigate insulating samples. Therefore, an electron of an occupied sample state  $\psi_n$  whose energy lies in between  $E_F$  and  $E_F - eV_b$  has a possibility to tunnel into the tip (Fig. 2.2).

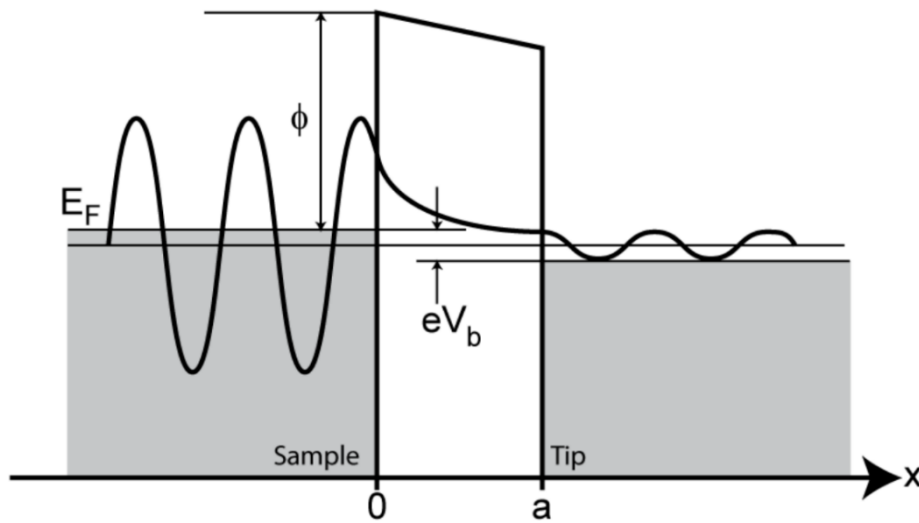


**Fig. 2.2:** Schematic illustration of the metal-vacuum-metal system showing the tunneling process from the sample into the tip at finite voltage.<sup>60</sup>

## 2. Experimental methods: theory and setup

Assuming that the energy of the tip state is lying close to the Fermi level, the probability of an electron tunneling from this tip state to the surface of the sample is:

$$|\psi_n(0)|^2 e^{-2\kappa a} \text{ with } \kappa = \sqrt{\frac{2m\phi}{\hbar}} \quad (2.6)$$

The sum over all sample states between  $E_F$  and  $E_F - eV_b$  leads to the formulation for the tunneling current:

$$I_t \propto \sum_{E_F - eV_b}^{E_F} |\psi_n(x)|^2 \quad (2.7)$$

When assuming a constant local density of states (LODS) for the tip, as well as low voltages and  $T = 0$ , we can get equation 2.8 from equation 2.7:

$$I_t \propto V_b \rho(0, E_F) e^{-2\kappa a} = V_b \rho(0, E_F) e^{-\frac{2a\sqrt{2m\phi}}{\hbar}} \quad (2.8)$$

where  $\rho(0, E_F)$  is the local density of states (LDOS) close to the Fermi level. Assuming that the LDOS near Fermi level is almost constant, the tunneling current is proportional to the voltage and the LDOS, but it has an exponential dependence on the distance between the sample and the tip.

Taking into account that tip and sample have different wave functions, there is a matrix element introduced by Bardeen,<sup>61</sup> which describes the overlap of the two wave functions. Tersoff and Hamann<sup>62</sup> considered a tip represented by a s-type wave function and evaluated the matrix element. If the bias voltages  $V_b$  is small, the tunneling current  $I_t$  is directly proportional to the LDOS of the sample.

$$I_t \propto V_b e^{-2kR} \rho_{tip}(E_F) \rho_{sample}(E_F, \gamma_0) \text{ with } k = \frac{\sqrt{2m\phi_t}}{\hbar} \quad (2.9)$$

where  $R$  is the effective tip radius,  $\phi_t$  the barrier height and  $\gamma_0$  the center of curvature of the tip. Consequently, an STM image does not show the true topography of the surface, but a convolution of the LDOS and the topography.

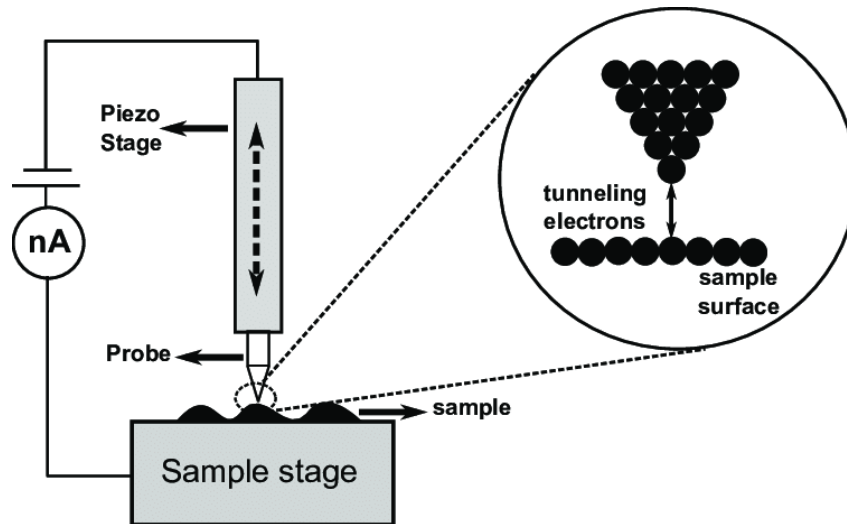


**Fig. 2.3:** Simplified working diagram of STM.<sup>63</sup>

Fig. 2.3 shows the working principle of a typical STM. First, the tip is brought close to the sample. A bias voltage is applied between the tip and sample, resulting in a tunneling current. The piezo can drive the tip to move above the sample surface. In different operation modes, the height of the sample or the tunneling current serve as the different signals for imaging.

### 2.1.2 Scanning modes

First the tip is approached to the surface by a piezo tube scanner. By applying a bias voltage, the current is recorded until the tip is close enough to the surface. In STM, two important scanning modes are classified: constant current mode and constant height mode (Fig. 2.4).

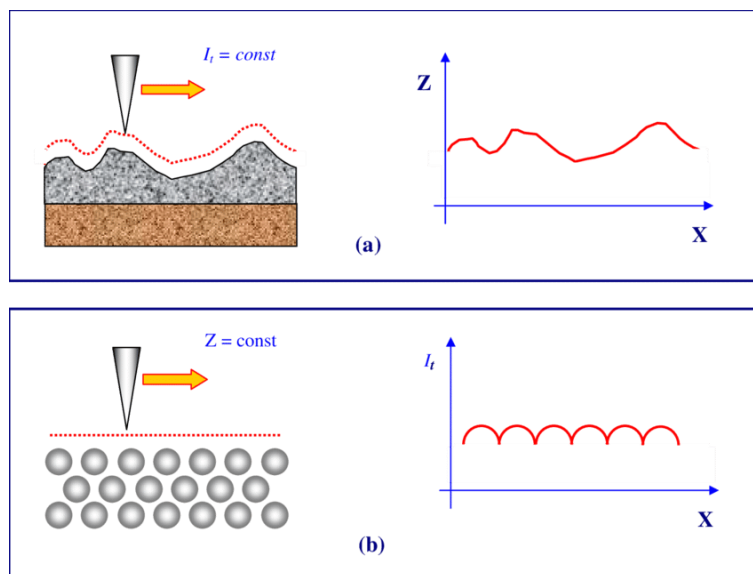


**Fig. 2.4:** Illustration of the two STM operation modes: (a) The constant current mode. (b) The constant height mode.<sup>64</sup>

## 2. Experimental methods: theory and setup

The constant current mode is the most common mode. By using a feedback loop, the height of the tip can be adjusted continuously. Once a tunneling current is chosen, it is held constant by adjusting the tip height. A topographic image is obtained *via* recording the movement of the tip.

In the constant height mode, the average height between the tip and the surface is constant and changes of the tunneling current are recorded. With this mode, a feedback loop is not necessary and higher scanning speeds can be applied to the scanning. But there is risk that the tip may crash into the surface.

### 2.1.3 Experimental setup

A home-built UHV system is combined with a variable-temperature STM (Aarhus 150 SPECS Surface Nano Analysis GmbH),<sup>65,66</sup> which is commercially available. The UHV system contains two chambers: the STM chamber and the preparation chamber. There is a vertical gate valve separating the two chambers. The preparation of the sample, the cleaning of the surface by cycles  $\text{Ar}^+$  sputtering and annealing, the physical vapor deposition (PVD) of metal atoms on the surface through a home built metal evaporator, is done in the preparation chamber. To investigate the surface with atomic precision, the sample is transferred from the preparation chamber to the STM chamber by using the manipulators.

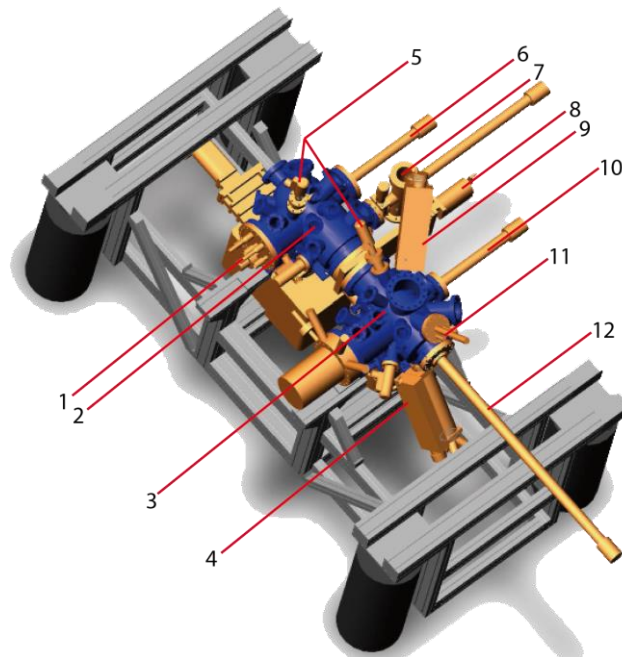


**Fig. 2.5:** Setup of the UHV chamber. (1) The variable-temperature Aarhus STM, (2) STM chamber, (3) preparation chamber, (4) OMBE, (5) argon sputter guns in two chambers, (6, 10, 12) manipulators, (7) loadlock, (8) gate valve, (9) metal evaporator, (11) sample parking stage.<sup>67</sup>

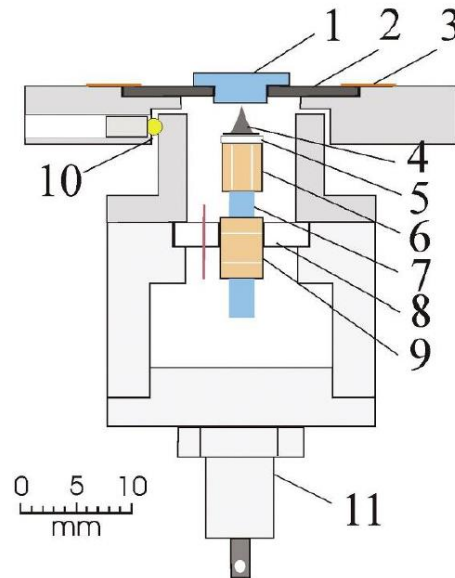


**Fig. 2.6:** Cross-section side view of the Aarhus STM. Schematic of Aarhus 150 VT-STM. (1) Sample. (2) Molybdenum sample holder. (3) Clamps. (4) Tip. (5) Tip holder. (6) Scanner tube. (7) SiC rod. (8) Mount inchworm motor. (9) Piezo of inchworm motor. (10) Insulating quartz balls. (11) Zener diode for possibility of tip heating.<sup>65</sup>

Fig. 2.6 shows the sample (1) on a molybdenum plate sample holder (2), which is fixed by two springs (3). The quartz balls (10) create a separation of the top part from the STM scanner thermally and electrically, and the top plate with the scanner is mounted on an aluminum block whose temperature could be adjusted by liquid nitrogen cooled finger and/or a heating Zener diode (11). The tip (4) is held by the tip holder (5) which is fixed on the top of the scanner tube (6), together with the SiC rod (7) and inchworm piezo motor (9). When suitable voltages are applied to the inchworm motor with piezo elements, the tip can move across several mm to coarsely approach the sample surface. Once the tunneling distance is achieved and scanning is initiated, the piezo system will receive the signal of the feedback loop to keep a constant current. The whole STM system is suspended by springs during investigation in order to reduce mechanical noise in combination with other mechanical damping systems.

## 2. Experimental methods: theory and setup

To fabricate the tip, a tungsten wire is immersed into 2M NaOH aqueous solution, then processed through electrochemical etching by applying 2.5 V - 3.5 V direct current between the aluminum cathode and the anode of tungsten wire (Fig. 2.7). The related electrochemical reaction is:

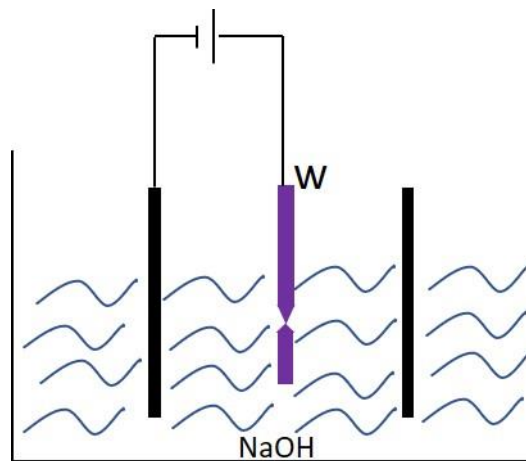


**Fig. 2.7:** Sketch of the etching process of tungsten tip.

After etching, the tip is cleaned with deionized water. The tip is stable even when it is exposed to air because of the formation of a thin oxide layer on surface. After the tip is mounted, its oxide layer will be removed through sputtering with argon ions.

## **2.2 Electrospray-controlled ion beam deposition**

The operation principle of our current system is to generate molecular ions from electrospray, efficiently guide them into UHV and purify them by using a mass selective spectrometer before deposition onto the substrate. Compared to other techniques like OMBE or drop casting, ES-CIBD has huge advantages regarding its application to diverse chemical species, on the fly identification and purification of components, controllable landing energy and quantification of the deposited species. Because of its advantages, ES-CIBD is one of the most promising methods for atomically clean deposition of molecules in UHV. But at the same time, ES-CIBD is by far more complex than other techniques.

With OMBE's crucible, a Knudsen cell filled with molecules is used. After being heated, the molecules will be deposited onto the substrate. Drop casting means deposition of dissolved molecules by employing a pipette. On the other hand, ES-CIBD is made up with a large differentially pumped vacuum systems, complex ion guides, extensive electronics and a tremendous parameter space. A lot of solvents and additives are involved in the optimization of the recipes for the solutions for the molecules. Besides different spray modes, emitters, solution flow rates, spray voltages and capillary heating temperature, the settings of all employed ion guides including the mass spectrometer as well as the landing energy play important roles in the experiments. Most of the ion guide settings can be preemptively estimated from the mass to charge ratio of the desired ion. In order to increase the usability of the machine, a sophisticated control over electronics and the development of corresponding software is very helpful. One can also refer to previous parameters used in prior depositions of similar molecules. The optimization of suitable solvent-molecule systems can be very time consuming foregoing the actual electro spray process.

Under some circumstances, for the deposition of simple molecules, OMBE and drop casting can be more straightforward. However, ES-CIBD can extend the range of accessible molecules, especially regarding size and thermal stability. Additionally, it is an important deposition technique, which can be used when the purity of sample is uncertain.

## ***2. Experimental methods: theory and setup***

### **2.2.1 Electro spray ionization (ESI)**

In recent decades, in the field of mass spectrometry, the generation of gas phase ions from nonvolatile compounds attracts a lot of interest.<sup>68</sup> Over the years, people have investigated some different techniques: electron impact ionization, fast atom bombardment, laser desorption techniques like matrix assisted laser desorption ionization (MALDI), and electrospray ionization (ESI).<sup>68,69</sup> Additionally, some other related ambient pressure ionization techniques are employed.<sup>70</sup> Here, electrospray ionization was used because of its capability to deposit organic molecules which are difficult to be deposited by using OMBE regarding their size and thermal stability.<sup>71</sup> The mass range is almost unlimited and the chemical specificity is not high when employing ESI as ionization technique.<sup>72-74</sup> Additionally, it is the most widely used technique in mass spectrometry, as well as in preparative mass spectrometry by now.<sup>75,76</sup> A simple ESI source is made up by just few components (see Fig. 2.8). Typically a syringe with a pump can be considered as a start, to provide a solution, in which the analyte molecules are dissolved. A small capillary which is made from silica or metal is used as a typical emitter. A high voltage (HV) source is used to provide the solution with a well-defined potential. To generate a strong electric field, the solution filled tip of the emitter is set in front of a counter electrode. Charge carriers store up on the liquid's surface where electrostatic forces compete with capillary and gravitational forces. Sir Geoffrey Taylor found that in this geometry the shape of the solvent's surface alters from an ellipse to a cone. The corresponding Taylor cone ejects small charged droplets as spray.<sup>77</sup> In order to simplify the description, we will describe only the positive electrospray modes and the resulting positive ions. Negative electrospray modes follow similar mechanisms, but are less common.

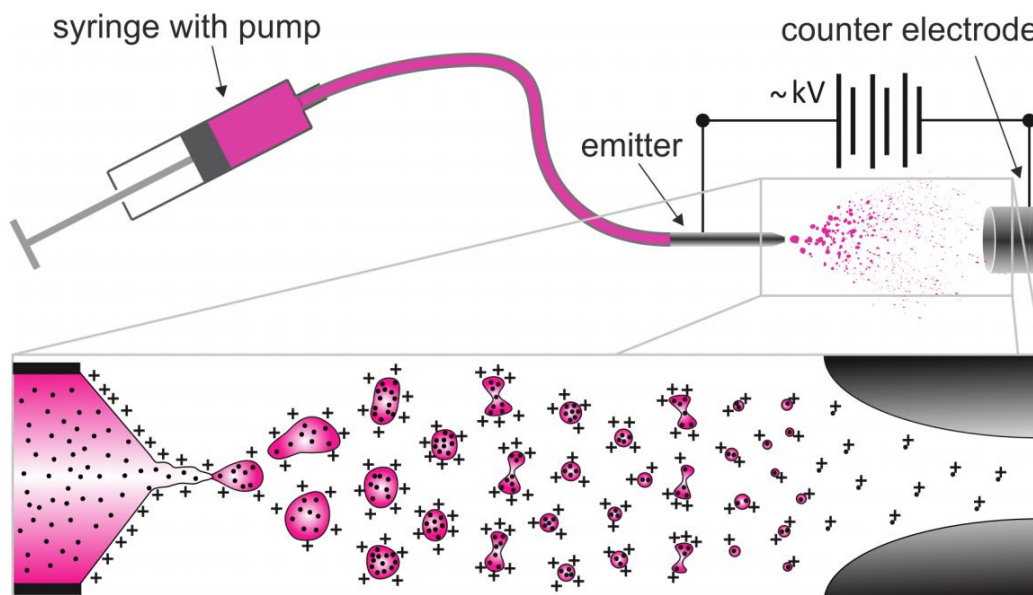


**Fig. 2.8:** Sketch of a simple ESI source, consisting of a syringe with a pump, which supplies a dissolved analyte (purple) to an emitter. From<sup>78</sup> with modifications.

### 2.2.2 Overview over the combined ES-CIDB and VT-STM setup

In Fig. 2.9, the variable temperature STM combined with the ES-CIDB is illustrated. The overview depicts the previously described STM chamber in green with the corresponding preparation chamber in blue. Both chambers are separated by a gate valve to avoid contamination caused by preparations via an OMBE and a metal evaporator, or sputtering and annealing cycles within the preparation chamber. The transfer manipulators (cyan) can be used for sample transport. The whole STM system was described in more detail previously.

## 2. Experimental methods: theory and setup

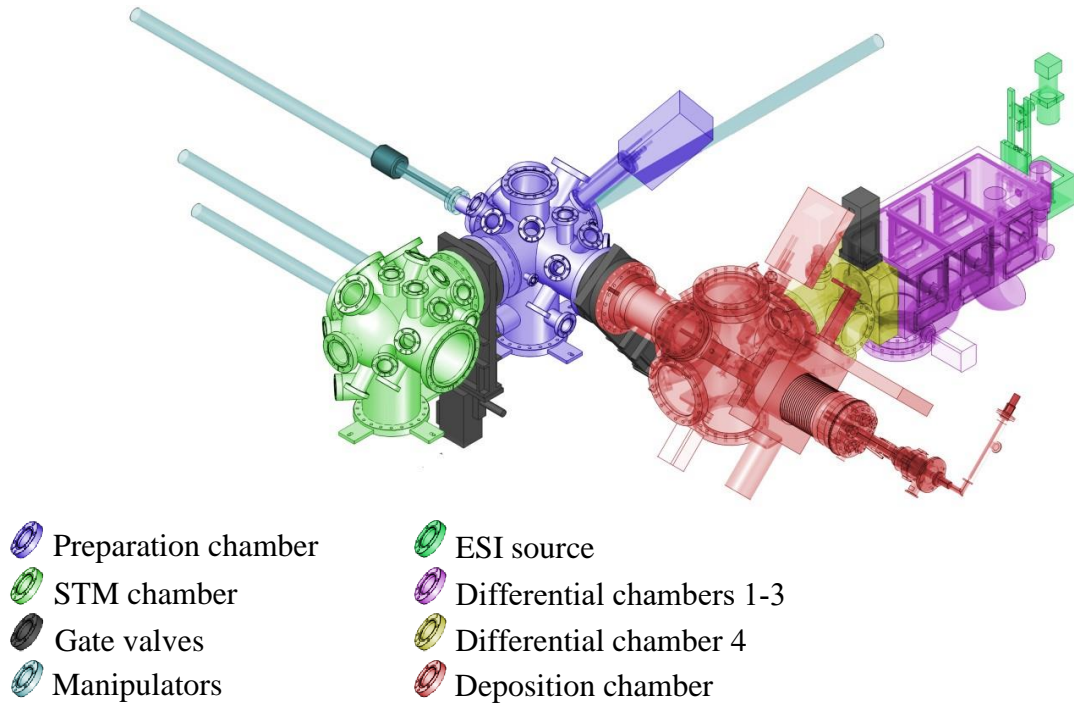


**Fig. 2.9:** Overview of the entity of ES CIBD attached to a VT STM. For illustrative reasons, the vacuum chambers are depicted without attachments.<sup>78</sup>

The ES CIBD is attached to the preparation chamber by a gate valve to avoid contamination. Besides, the separation can guarantee independent maintenance and bake-out procedures without influencing the vacuum of both devices. The ions are generated from the ESI source (green) and transported via the low vacuum section (purple) consisting of three differentially pumped vacuum chambers. The three vacuum regimes are distributed within an aluminium box which are divided by modular walls. To modify and maintain this part of the ES CIBD, one can routinely vent it to atmospheric pressure. In order to get a proper base pressure, the UHV section requires to be pumped with a subsequent bake-out and can be separated from the lower vacuum via an in-beam gate valve. The first UHV chamber (yellow) operates as a fourth differentially pumped chamber and is followed by the deposition chamber (red). The last ion optic of the ES CIBD ends just a few centimeters behind the connecting flange between chamber 4 and deposition chamber. Therefore, the actual whole system of ES CIBD is not much larger than the green, purple and yellow chamber together. The deposition chamber is not exclusively used for ES CIBD but also has a sputter gun, leak valves and a residual gas spectrometer. The deposition stage can rotate the sample and adjust it in x, y, z by a few cm.

## ***2.2 Electrospray-controlled ion beam deposition***

The temperature of the sample in the deposition stage can reach  $> 800$  K by electron bombardment heating or be cooled by liquid Nitrogen or liquid Helium.

## 3. Results and discussions

### 3.1 Depositing Molecular Graphene Nanoribbons on Ag(111) by Electrospray Controlled Ion Beam Deposition: Self-assembly and On-Surface Transformations

#### 3.1.1 Introduction

One-dimensional GNRs are interesting carbon-based materials owing to their potential use as components for devices in the next post-silicon technology. The large tunability in electronic and structural properties, mostly determined by the atomic structure of their edge, makes it possible to use them as active elements in nanoelectronic devices such as high performance field effect transistors,<sup>79–81</sup> diodes,<sup>82</sup> or as metallic interconnects.<sup>83</sup>

For such industrial implementation, it is highly necessary to control their chemical structure and morphology down to the atomic level. However, such a degree of precision cannot be achieved by current top-down approaches.

Recently atomically well-defined GNRs of various widths and edge structures can be synthesized using a bottom-up approach based on surface-assisted polymerization of suitable precursors. To this end the most widely used on-surface reaction is the Ullmann-type coupling reaction, which is the surface-assisted C-C homocoupling of aryl-halide structures. Therefore, specially designed molecular precursors, once deposited on a metallic substrate produce GNRs after thermally activated polymerization and subsequent cyclodehydrogenation. This allows growing for example GNRs with armchair, zigzag or chiral edges,<sup>84–87</sup> GNRs of different widths and electronic bandgap sizes,<sup>88–93</sup> GNRs with dopant heteroatoms<sup>94–98</sup> and GNRs with functional groups.<sup>99,100</sup>

In Fig. 3.1a we can see an example of the different steps in the Ullmann coupling reaction.<sup>101</sup> At 300 K, monomers of 4,4'-dibromo-*para*-terphenyl (Br-(Ph)<sub>3</sub>-Br) debrominate on a Cu(111) surface, and a polymeric organometallic intermediate is formed. The intermediate includes biradical terphenyl (Ph)<sub>3</sub> units that are connected through C-Cu-C bonds.

Recently, it was also shown that certain GNRs allow the lateral fusing<sup>88</sup> and synthesis via surface-assisted coupling of molecular precursors into linear polyphenylenes and their subsequent cyclodehydrogenation.<sup>84</sup>

### 3. Results and discussions

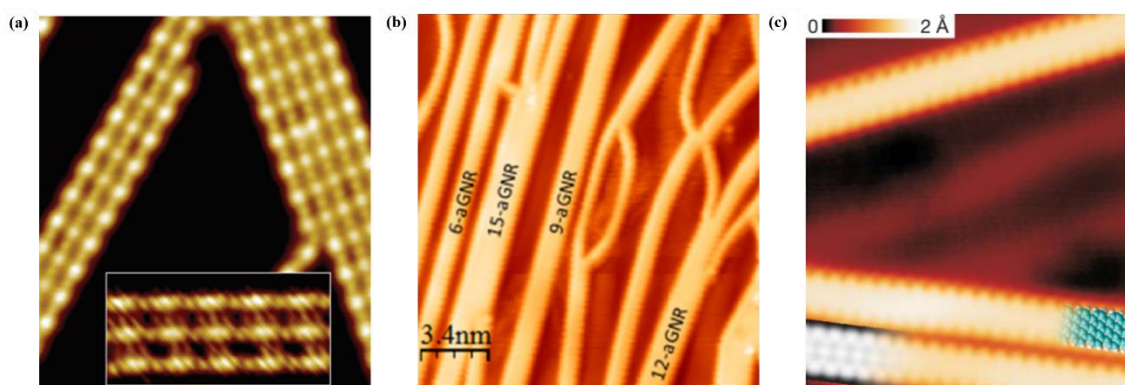


**Fig. 3.1: On-surface synthesis of GNRs.** (a) STM image of the sample annealed to 300 K. Br atoms lying between the linear periodical structures.<sup>101</sup> (b) STM image of armchair type GNRs with varying widths obtained after laterally fusing poly-(para-phenylene) chains.<sup>88</sup> (c) High-resolution STM image with partly overlaid molecular model (blue) of the ribbon.<sup>84</sup>

However, in general it is highly difficult to control the length, width and homogeneity of GNRs precisely and additional species tend to be present on the surface (most likely halogen atoms). Therefore, a technique that allows the deposition of well-defined, defect-free GNRs on-surfaces would be highly desirable.

In the following chapter we investigate the deposition of atomically-precise and homogenous GNRs on Ag(111) by ES-CIBD. STM measurements under UHV conditions evidence that the deposited GNRs land intact on the Ag(111) surface (morphology of the molecules is preserved) while any contamination or additional species are absent. In addition, a statistical analysis of the GNR length for increasing sample annealing temperatures (from RT to 583 K) reveals that GNRs remain intact up to 443 K, where the end groups are detached from the GNR. The lateral silyl groups split off at 483 K. In addition, beyond 523 K we observe that a chemical reaction that takes place at the oxygen termination, yielding the formation of longer GNR chains, indicative of the polymerization of the deposited GNRs molecules.

### ***3.1 Depositing Molecular Graphene Nanoribbons on Ag(111) by Electrospray Controlled Ion Beam Deposition: Self-assembly and On-Surface Transformations***

#### **3.1.2 Sample Preparation**

For the ES-CIBD experiment, a stock solution ( $3.23 \times 10^{-4}$  g/ml) of the synthesized graphene nanoribbons was prepared by dissolving the GNR powder in THF (tetrahydrofuran). 25  $\mu$ l 0.5% TCA in water (in weight) trichloroacetic acid was added into 250  $\mu$ l THF. Then, 125  $\mu$ l stock solution was added to give a final concentration of  $1.0 \times 10^{-4}$  g/ml. Subsequently, positively charged gas-phase ions of the GNRs were generated by our home-built ES-CIBD apparatus, charge +2 for molecules; voltage 3.5 kV on the emitter, flow rate 60~90  $\mu$ lh<sup>-1</sup>, current up to ~55 pA, deposition time about 1.5 hours. Before the deposition in UHV, the composition of the ion beam was monitored by a digital quadrupole mass spectrometer and filtered by applying an additional DC offset. The deposition took place in a UHV chamber with a base pressure of  $9 \times 10^{-10}$  mbar. The landing energy of the molecular ion beam was 2 eV per charge to avoid fragmentation. Before the deposition, the Ag(111) single crystal was cleaned by repeated cycles of Ar<sup>+</sup> sputtering and subsequent thermal annealing. The sputter gun ionizes argon and accelerates the argon ions with a high voltage of 1 kV and an emission current of 15 mA. The adsorbates and impurities are removed by bombarding the surface with Ar<sup>+</sup>, but the top layers of the surface atoms are also partly removed, leaving a rough surface. The subsequent annealing in vacuum to 700 K can heal the Ag(111) surface to get a clean and atomically flat surface eventually.

After the cleaning, the substrate was transferred to the ES-CIBD chamber. After dosing molecules, the sample was transferred to the STM chamber to do the analysis. STM measurements were conducted in a range between 190 K to 110 K. All voltages refer to the sample bias with respect to the tip. All STM measurements were performed with a chemically etched W tip. The STM data analysis was performed using WSxM.

An important advantage of this approach is the possibility of extracting specific ions from a mixture using the mass-filtered deposition capability of ES-CIBD. The m/z filtering quadrupole is initially tuned so that only the desired molecules make their way to the substrate. STM imaging of the molecules deposited in this way reveals structures corresponding to the selected molecules (Fig. 3.3).

### 3. Results and discussions

Here, we employed a monodisperse N-doped conjugated polyaromatic species (shown in Fig. 3.2), which is obtained by multistep organic synthesis in solution.<sup>102</sup> The differences of the self-assembly with varying coverage at RT were investigated as well as the behavior of the molecules as a function of the annealing temperature on the metal surface Ag(111) in UHV.

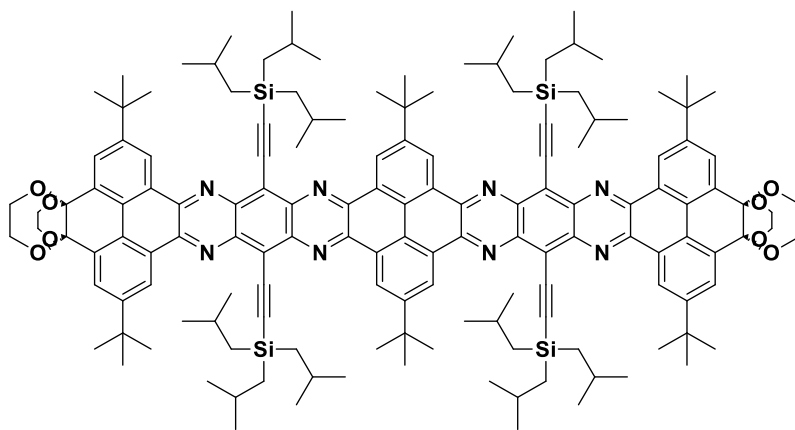


**Fig. 3.2:** Chemical structure of NR10 ( $C_{148}H_{190}N_8O_8Si_4$ ). Its molecular weight is 2320 g/mol.

### 3.1 Depositing Molecular Graphene Nanoribbons on Ag(111) by Electrospray Controlled Ion Beam Deposition: Self-assembly and On-Surface Transformations

#### ESI deposition onto Ag(111)

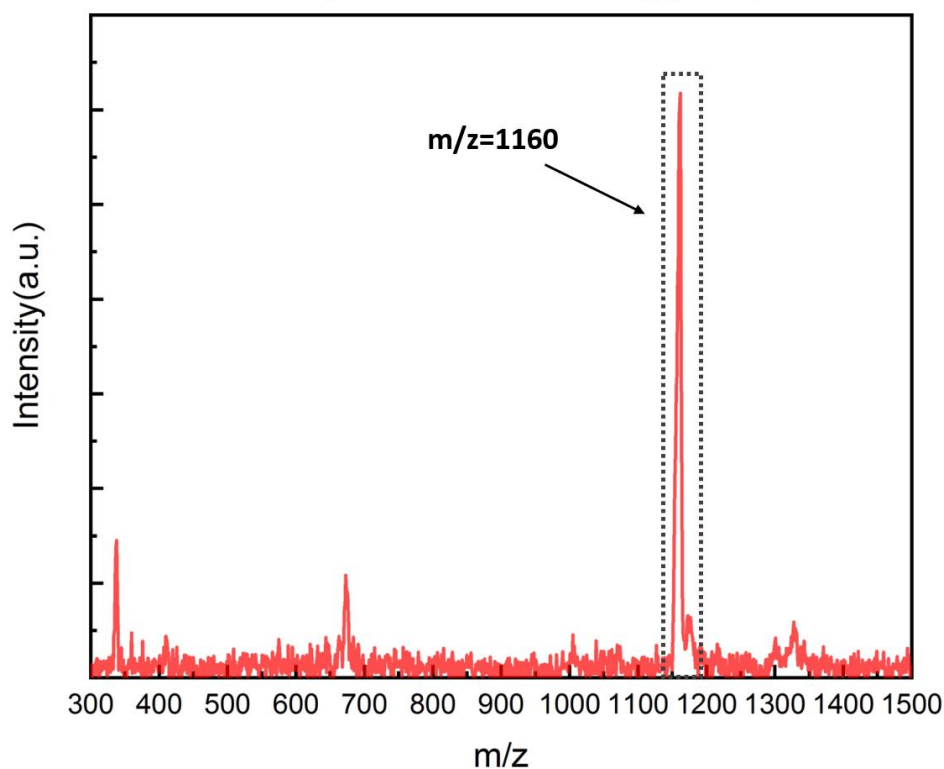


**Fig. 3.3:** Mass spectrum of NR10 in THF solution. The selected m/z ratio for ESI deposition is marked by the dashed rectangle.

#### 3.1.3 Coverage-dependent self-assembly

To investigate intermolecular interaction we studied the self-assembly at different coverages of NR10 molecules deposited onto an Ag(111) substrate held at RT.

### 3. Results and discussions

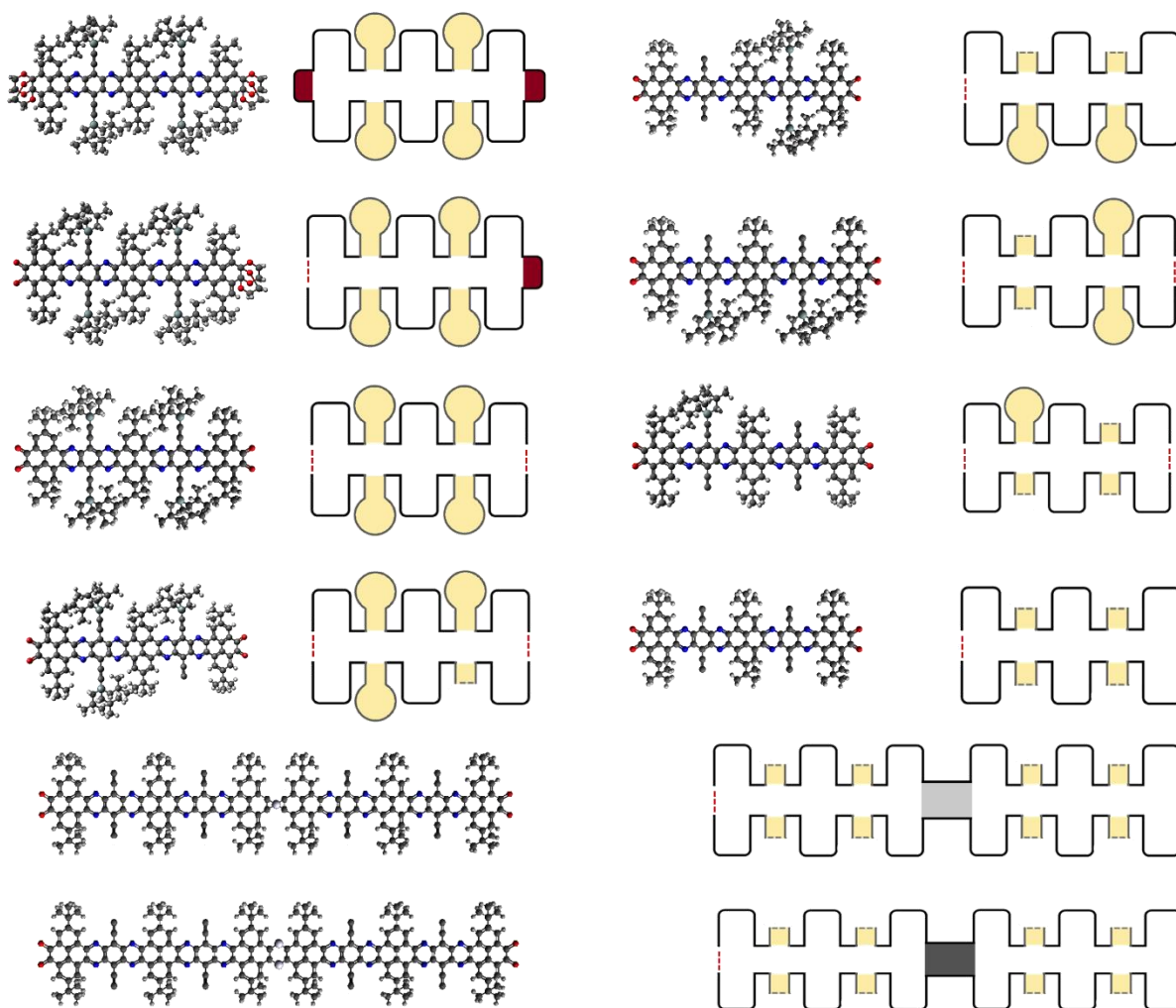


**Fig. 3.4:** Molecular models and their corresponding schematic models, used in order to show the self-assembly of molecules in the STM images clearly.

### 3.1 Depositing Molecular Graphene Nanoribbons on Ag(111) by Electro spray Controlled Ion Beam Deposition: Self-assembly and On-Surface Transformations

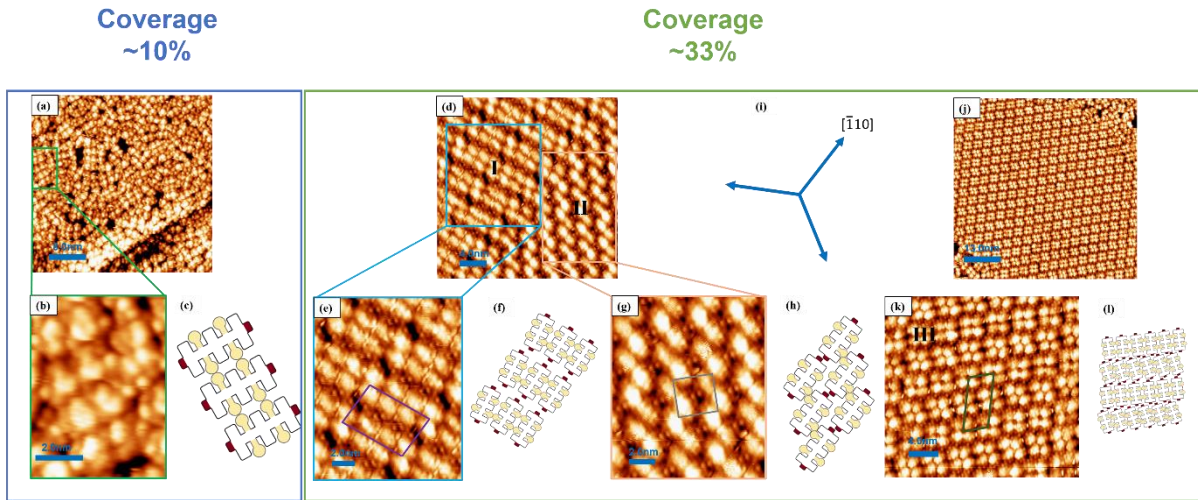


**Fig. 3.5: Coverage-dependent self-assembly of NR10 deposited onto Ag(111) held at RT.** (a) STM image of irregularly assembled molecules after deposition of  $4 \times 10^{-13}$  mol. ( $T_{STM} \sim 170$  K,  $U_s = 2.3$  V,  $I_t = 0.04$  nA). (b) Magnified image of the green area in (a) showing a small section with locally regular assembly. (c) Structural model of the assembly shown in (b). (d, j) STM images of three different self-assembled phases obtained after deposition of  $1.3 \times 10^{-12}$  mol. (d:  $T_{STM} \sim 153$  K,  $U_s = 2.1$  V,  $I_t = 0.14$  nA; j:  $T_{STM} \sim 170$  K,  $U_s = 2.1$  V,  $I_t = 0.14$  nA). (e, g) Magnified images of the blue/orange area in (d) showing phases I and II. (k) Magnified image of (j) showing phase III. The unit cells are indicated in the images (e, g, k) Respective structural models of the assembly of the phases I,II,III are shown in (f, h, l). (i) The blue star indicates the high symmetry directions of the Ag(111) substrate.

Deposition of  $4 \times 10^{-13}$  mol yields a surface with a low molecular coverage ( $\sim 10\%$ ). The molecules agglomerate into irregularly assembled islands, as shown in the STM image in Fig. 3.5a. Small sections with regular assemblies can be found. Such a section is marked with green in Fig. 3.5a and shown in Fig. 3.5b. The respective structural models of this assembly are shown in Fig. 3.5c. In order to study the influence of density of molecules, the coverage was increased by 3.25 times (i.e.  $1.3 \times 10^{-12}$  mol deposition). This preparation leads to substantially different behavior. In contrast to the irregular assembly for lower coverages, now we observe a regular assembly of the molecular units (Fig. 3.5d and Fig. 3.5j). Three different phases were observed (Figs. 3.5e,g,k). Zoom-ins and structural models are shown in Figs. 3.5f, h, l. The single units comprising these structures all exhibit four bright protrusions, which are assigned to the protruding TIBS groups of NR10. The respective unit cells have dimensions of 6.0/2.9/11.0 nm times 4.0/2.9/23.6 nm with an angle of  $97^\circ/90^\circ/75^\circ$  in Figs. 3.5e,g,k. We can identify part of NR10 molecules orientated along the high symmetry directions of the substrate

### ***3. Results and discussions***

in Fig. 3.5g, which is the magnified image of the orange area of Fig. 3.5d, superimposed with corresponding molecular models in Fig. 3.5h.

In the ESI process, the molecules are deposited as doubly charged cations. However, their charge state after adsorption on the metallic substrate is unknown. However, as the intermolecular spacing is rather small, it is likely that Coulomb repulsion does not play a major role and the molecules do not carry a significant amount of charge.

#### **3.1.4 Chemical reactivity of NR10 on Ag(111)**

To investigate the chemical reactivity of NR10 on Ag(111) upon annealing, we performed temperature controlled heating experiments. We analyzed the distribution of different products of thermally induced reactions as a function of temperature. This annealing treatment alters the assembly of the NR10 species (and its reaction products) and induces different type of chemical reactions, i.e. cleavage of side groups, as well as intermolecular coupling.

### 3.1 Depositing Molecular Graphene Nanoribbons on Ag(111) by Electro spray Controlled Ion Beam Deposition: Self-assembly and On-Surface Transformations

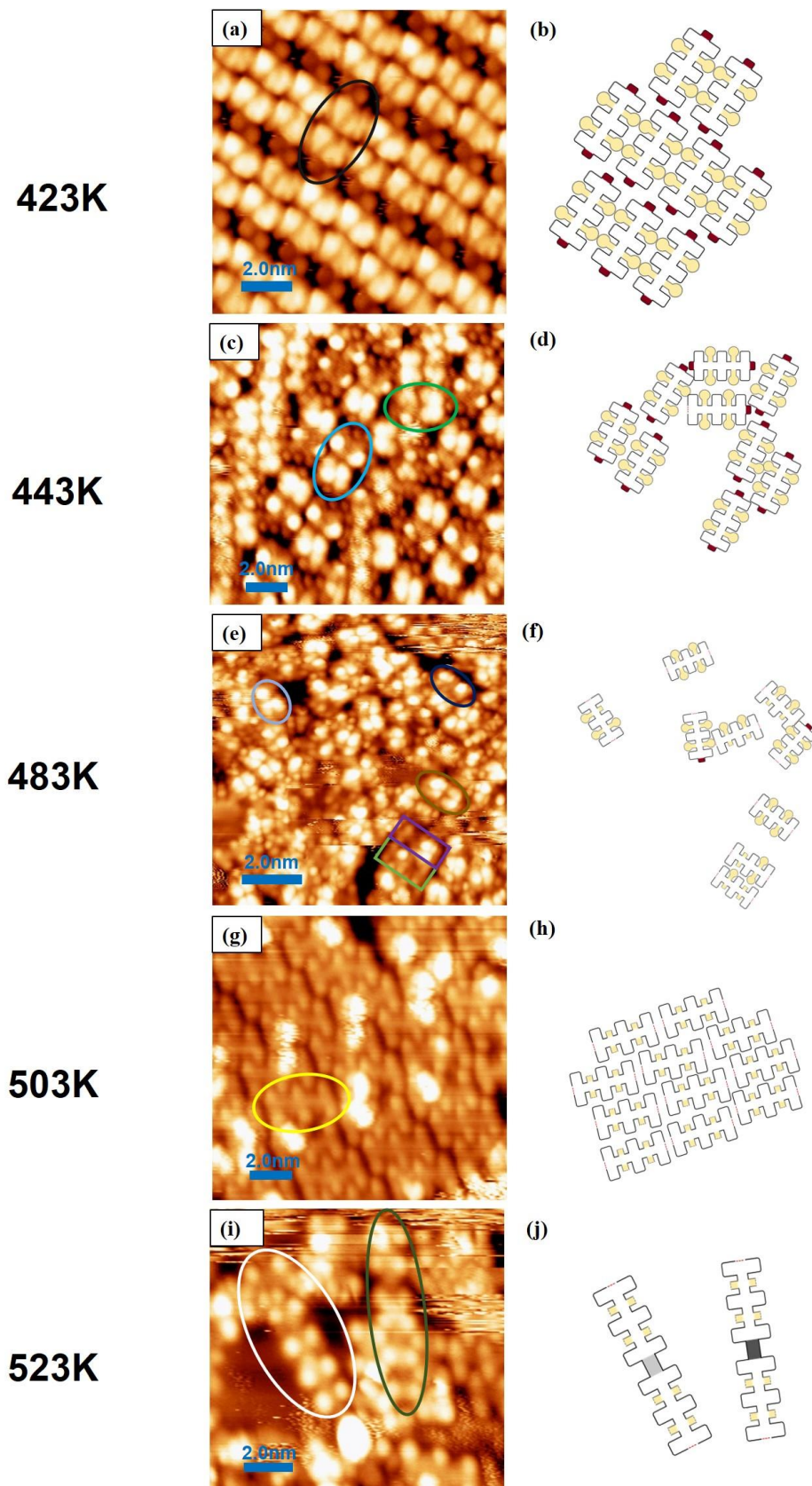


**Fig. 3.6: NR10/Ag(111) assembly and chemical reactivity by thermal annealing.** (a, c, e, g, i) STM images of NR10 and its reaction products after annealing to 423 K, 443 K, 483 K, 503 K, 523 K, respectively (a:  $T_{STM} \sim 160$  K,  $U_s = 2.1$  V,  $I_t = 0.12$  nA c:  $T_{STM} \sim 142$  K,  $U_s = 2.1$  V,  $I_t = 0.1$  nA e:  $T_{STM} \sim$

### 3. Results and discussions

145 K,  $U_s = 2.1$  V,  $I_t = 0.13$  nA g:  $T_{STM} \sim 110$  K,  $U_s = 2.1$  V,  $I_t = 0.11$  nA i:  $T_{STM} \sim 120$  K,  $U_s = 2.1$  V,  $I_t = 0.08$  nA). The outlines in the images mark the chemical units that form the respective assemblies. **(b, d, f, h, j)** Models representing the respective structures in (a, c, e, g, i).

NR10 molecules were deposited on a Ag(111) surface at room temperature (RT, 300 K). The sample was then subjected to annealing steps (typically 10 minutes) and cooled back down for STM measurements after each annealing step. Figs. 3.6 (a, c, e, g, i) show representative images of the surface after annealing to 423 K, 443 K, 483 K, 503 K, 523 K respectively.

Fig. 3.6a shows the STM image of NR10 deposited onto Ag(111) after annealing to 423 K with molecular models in Fig. 3.6b, from which we can clearly identify NR10 molecules clustered together with the same structure as deposited at RT.

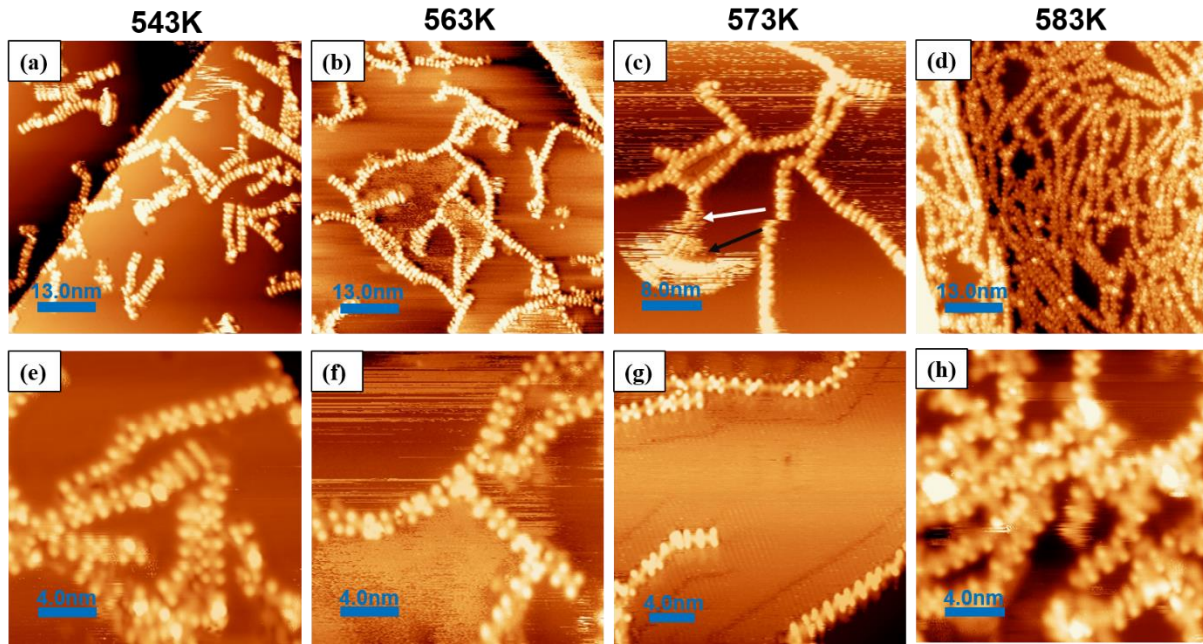
In Fig. 3.6c, STM investigations were carried after annealing to 443 K, showed a disordered assembly of NR10 with molecular models in Fig. 3.6e, in which the different products are highlighted by blue and green. The end group of the molecule starts to be deprotected. For the molecule outlined in green one can notice the lack of contrast on the left end vs the circular small protrusion on the right, which indicates a deprotection of the left end group.

Fig. 3.6e shows an overview in which we can discern some distinct molecules, for instance, a NR10 molecule with one TIBS group left (green square), a NR10 molecule with two TIBS groups left (outlined in square). That indicates that the TIBS groups have partially split off from the original NR10 molecules step by step with the corresponding molecular models in Fig. 3.6f.

Subsequent further annealing to 503 K, reveals that molecules without any TIBS groups furnish the surface (shown in Fig. 3.6g with the proposed molecular models in Fig. 3.6h). We can see that the molecules are well ordered and densely packed on the metal surface. A single molecule is circled in yellow.

A representative STM image after further annealing to 523 K is displayed in Fig. 3.6i, from which we can distinguish dimers from the product molecule presented in Fig. 3.6j. Two dimers are outlined, which confirmed that further heating modestly promoted dimerization.

### 3.1 Depositing Molecular Graphene Nanoribbons on Ag(111) by Electro spray Controlled Ion Beam Deposition: Self-assembly and On-Surface Transformations



**Fig. 3.7: On-surface polymerization of NR10 on Ag(111) by thermal annealing.** (a, b, c, d) Overview of polymer chains after annealing to 543 K, 563 K, 573 K, 583 K, respectively (a:  $T_{STM} \sim 140$  K,  $U_s = 0.8$  V,  $I_t = 0.06$  nA b:  $T_{STM} \sim 160$  K,  $U_s = 2.2$  V,  $I_t = 0.09$  nA c:  $T_{STM} \sim 110$  K,  $U_s = 1.7$  V,  $I_t = 0.09$  nA d:  $T_{STM} \sim 160$  K,  $U_s = 1.8$  V,  $I_t = 0.09$  nA). (e, f, g, h) Magnified images of polymer chains after annealing to 543 K, 563 K, 573 K, 583 K, respectively. (e:  $T_{STM} \sim 140$  K,  $U_s = 1.4$  V,  $I_t = 0.14$  nA f:  $T_{STM} \sim 160$  K,  $U_s = 2.2$  V,  $I_t = 0.1$  nA g:  $T_{STM} \sim 133$  K,  $U_s = 1.5$  V,  $I_t = 0.03$  nA h:  $T_{STM} \sim 160$  K,  $U_s = 1.7$  V,  $I_t = 0.11$  nA).

Fig. 3.7 illustrates the on-surface polymerization of NR10 on Ag(111) upon thermal activation. GNR chains could be polymerized via Ullmann-type coupling before. In some recently developed protocols facilitation of the formation of the polymers and removal of the unwanted polymerization byproducts (like Br) proceeds at reduced activation temperatures by H-dosing treatment.<sup>103</sup> Different from Ullmann coupling reaction, the polymerization in our case is highly simplified because no halogen is present. The submonolayer coverage sample was annealed to 543 K, 563 K, 573 K, 583 K, respectively and subsequently cooled for the STM measurements. At heating temperature below 543 K, no well-defined polymer chains were observed. Instead, ordered or disordered islands as well as dimers were found as shown in Fig. 3.6i. After annealing at temperatures of 543 K, 563 K, 573 K and 583 K, individual 1D polymer chains could be observed in Fig. 3.7a b, c. Fig. 3.7e, f, g present high resolution STM images of a 1D chain at the corresponding temperature. In Fig. 3.7e, oligomers polymerized by 2, 3 or 4 monomers could be seen. After further annealing to 563 K, we can observe the formation of the longer chains as shown in Fig. 3.7b. In Fig. 3.7c, we heated the sample to 573 K, at which

### 3. Results and discussions

temperature the length of the chains is slightly increased. Interestingly large mobile sections of the chains could be observed, which indicate the formation of bonds between the monomers with different rigidity. The inflection points of the chain trajectory indicate a flexible yet robust pinning of the chain, which is mediated by a node structure. This is further discussed along with the node assignment in a later section. A dense network of polymer chains can be seen in Fig. 3.7d.

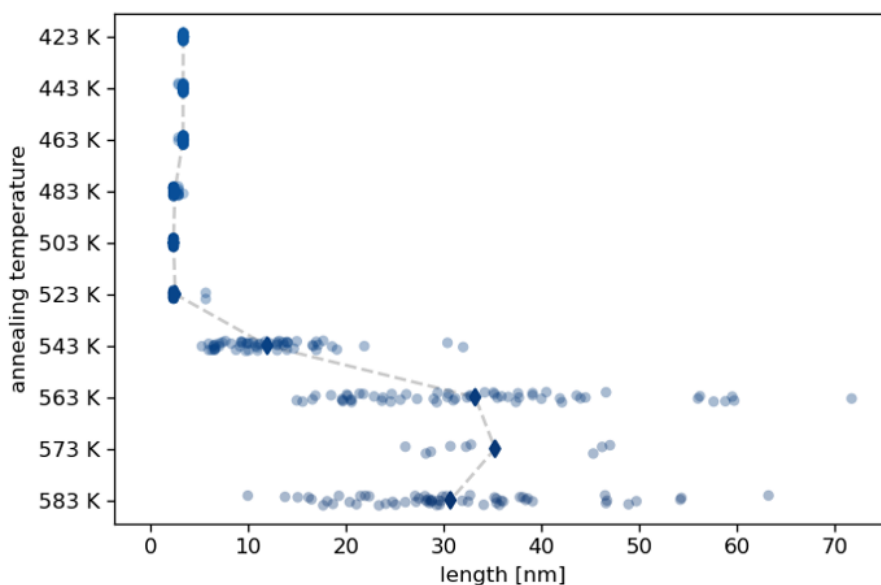


**Fig. 3.8: Statistical analysis:** The distribution of the lengths of the nanoribbons as a function of the annealing temperature. The dashed lines represent the average lengths at the corresponding annealing temperature.

A statistical analysis over the length of the products in dependence of the annealing temperature is displayed in Fig. 3.8. It reveals a maximum length of the products remaining around 3.4 nm below 423 K. By careful inspection we can deduce that the end groups cleaved off after the heat treatment to 443 K. This is illustrated by the green outline in Fig. 3.6c, where two altered end groups are resolved clearly in comparison with the intact ones. With increased annealing temperature to 483 K, more the molecules are shortened (indicative of end group deprotection, Fig. 3.6e). At 503 K, all the end groups from the molecules are cleaved off. Dimers occur at 523 K in Fig. 3.6i, as is also apparent in the statistical analysis. Longer oligomers can be seen in Fig. 3.7a after higher temperature annealing to 543 K. At higher temperatures, the polymer chains are longer than in the range of 563 K to 583 K. The dashed line in Fig. 3.8 indicates the

### 3.1 Depositing Molecular Graphene Nanoribbons on Ag(111) by Electro spray Controlled Ion Beam Deposition: Self-assembly and On-Surface Transformations

average lengths within this range, from which we can conclude that the length does not change significantly at this temperature interval.

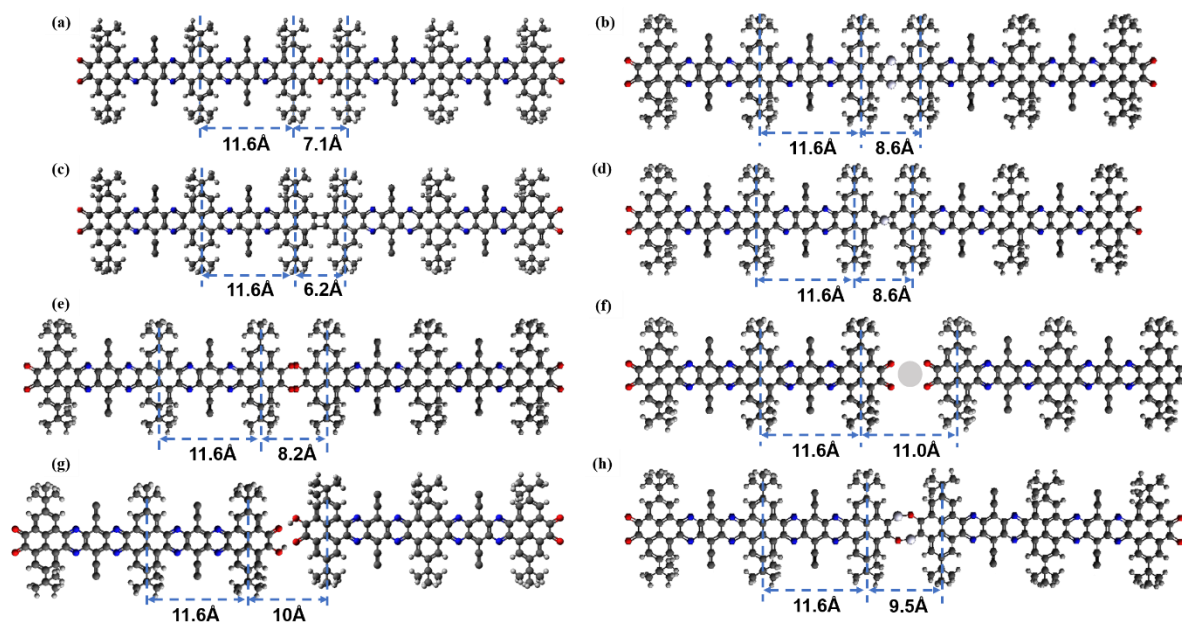


**Fig. 3.9: Tentative models proposed for the dimer motif.** The vertical blue dotted lines indicate the positions of the physically protruding <sup>t</sup>Bu groups, which are strong markers in the STM data. The distances determined from different proposed model structures for the bonding mechanism of the polymer chains are marked.

L. Zhang<sup>104</sup> investigated trimethylsilyl (TMS) terminated alkynes on metal surfaces, in which TMS groups cleaved off on Cu(111) at 400 K. Similarly to this, the abstraction of the TMS groups from the original precursor happened during the thermal activation reported by S. Kawai.<sup>105</sup> In our case, the onset of TIBS group abstraction occurred on Ag(111) at 483 K, which is indicated in Fig. 3.6e.

R. Zhang<sup>106</sup> reported the formation of an organo-silver framework comprising Ag adatom trimers on Ag(111) after 493 K annealing. After annealing this sample to 563 K, oligomers are formed via [2+2] cycloaddition, as in the model proposed in Fig. 3.9c. This also could be seen in C. Sánchez-Sánchez's work.<sup>107</sup> After a dehalogenation reaction, activated molecules undergo a [2+2] cycloaddition reaction to form the final nanoribbon at 475 K. On-surface polymerization on Au(111) was also investigated by Bay V. Tran,<sup>103</sup> in which two endocyclic

### 3. Results and discussions

C=C bonds were the linkers between the molecules to form the chains after annealing to 450 K.

D. Ada<sup>108</sup> observed that Cu adatoms were captured by the strongly electron-accepting ketone groups composing alternating PTO molecules and Cu adatoms. The diketone moiety was used as a functional “head” group for Ag coordination.<sup>109</sup> Similarly, the proposed model in Fig. 3.9f shows Ag adatoms bound by the strongly electron-accepting ketone groups and incorporated in metal–organic structure. Beside, we also propose two models with C-O-C and C-O-O-C for the polymer chains, which are shown in Fig. 3.9a and Fig. 3.9e.

In Figs. 3.9b and d, the C–Ag–C metal–ligand bonds are proposed in the polymer chain models, which is similar to the C–Cu–C linkages reported by Bay V. Tran.<sup>103</sup> The nodes with the hydrogen bonds and diagonal bonds were also proposed in Figs. 3.9g and h respectively.

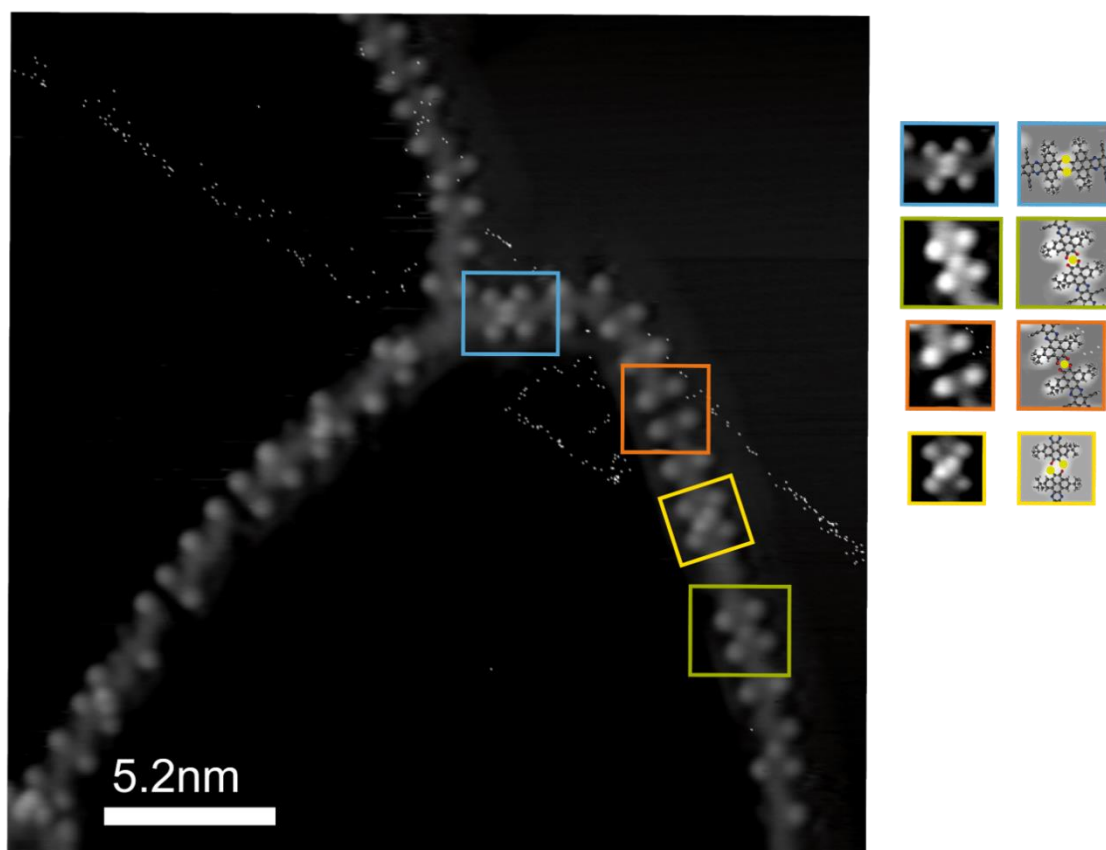


**Fig. 3.10:** Different coordination motifs and proposed models. C, N, O, H, and Ag atoms are depicted in black, blue, red, white, and yellow, respectively.

### 3.1 Depositing Molecular Graphene Nanoribbons on Ag(111) by Electrospray Controlled Ion Beam Deposition: Self-assembly and On-Surface Transformations

However, the proposed models (Figs. 3.9b and d) which represent 2 Ag atoms and 1 Ag atom of metal-coordinated bonds, respectively, exhibit distances of 11.6 Å and 8.6 Å. Thus, we propose that the observed polymeric chains are stabilized by metal-bound bridges. According to statistical analysis in Fig. 3.11, the average distances between two nearest bright protrusions amount to 1.19 nm and 0.84 nm, respectively. The experimental lengths are in excellent agreement with the distances determined from the proposed model structure for the bonding mechanism of the polymer chains, where the distances are 1.16 nm and 0.86 nm. In Fig. 3.10, 4 different metal-organic nodes are outlined in different colors and overlaid with corresponding models. The node outlined in blue is the C–Ag–C metal–ligand bond, which is proposed in Fig. 3.9b. The Ag atom coordination node can be imaged in different ways, which are outlined in green and orange. The node outlined in orange between two nearest bright protrusions is dark. In an earlier work,<sup>109</sup> a similar node is investigated with a distance of 1.1 nm between two neighboring protrusions. The distance is consistent with the statistical analysis in Fig. 3.11b, in which a distance of 1.1 nm can be observed. A diagonal node is observed in the STM image, which is outlined in yellow. The distance between two nearest bright protrusions is 0.95 nm, which is agreement with the value shown in Fig. 3.11b too.

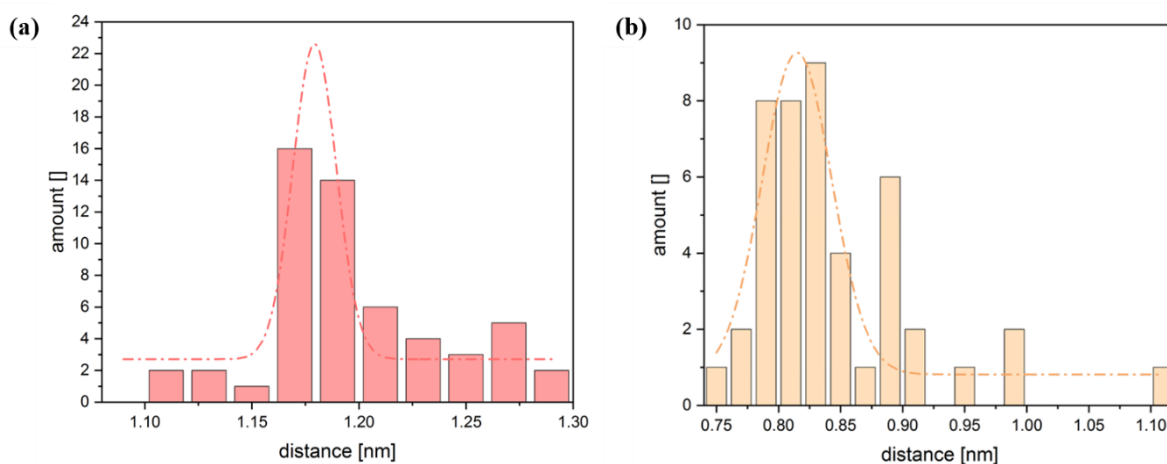


**Fig. 3.11: Statistical histogram:** (a) Distribution of the distances between two nearest bright protrusions within one monomer. (b) Distribution of the distances between two nearest bright protrusions between two monomers in the polymer chain. The average distances between two nearest bright protrusions amount to 1.19 nm and 0.84 nm, respectively.

#### 3.1.5 Summary and conclusion

In conclusion, we investigated the self-assembly and on-surface polymerization of NR10 molecules on Ag(111) surfaces under UHV conditions. Three coverage-dependent self-

### ***3. Results and discussions***

assembled phases stabilized by van der Waals interactions were observed. By employing thermal activation at different temperatures, we achieved an on-surface polymerization through organo-Ag bonds. Via a statistical analysis of the distances between neighboring bright protrusions, we can conclude that the observed polymeric chains are stabilized by Ag-coordinated bridges. Importantly, without undesired and hindering polymerization byproducts, the polymerization in our case is cleaner and simpler compared to the synthesis of GNR via Ullmann-type coupling. Moreover, the employed ES-CIBD method is regarded as a promising method for its capability to ionize very large or very fragile chemical species, especially organic molecules.

## 3.2 *PcZn(OH)<sub>8</sub>* on Ag(111)

### 3.2.1 Introduction

Metal–organic frameworks (MOFs) are crystalline porous materials composed by metal containing nodes and organic linkers. Recently, the research in MOFs is one of the fast growing fields in chemistry and materials, thanks to the tunability of structures and functions, large surface area, and ultrahigh porosity of MOF-based materials.<sup>110–112</sup> Now, 2D MOF nanosheets have gained extensive attention. Similar to other 2D nanomaterials, 2D MOF nanosheets can be used in many technological applications, including gas separation, energy conversion and storage, catalysis and sensing.<sup>113–125</sup> Therefore, 2D MOF nanosheets provide new opportunities in both fundamental studies and applications.

Unlike the top-down method of the exfoliation of layered MOFs, a bottom-up approach was employed with on-surface self-assembly to synthesize a single layer 2D-MOF.<sup>126</sup> The reaction between organic ligands and metals occurs on the interface. Therefore, the MOFs only grow in the confined two-dimensional interface region, leading to the formation of single nanosheets.<sup>127</sup> As a typical example of this process in the solid/vacuum interface, Zhang<sup>128</sup> and co-workers reported the synthesis of  $\text{Cu}_3(\text{C}_6\text{O}_6)$  nanosheets on a Cu(111) substrate. In their work, the BHO (benzenehexol) molecules are deposited on an atomically flat Cu(111) single crystal surface under UHV conditions. After annealing this sample above 400 K, a single layer 2D-MOF structure of  $\text{Cu}_3(\text{C}_6\text{O}_6)$  formed on the surface, as confirmed by high-resolution scanning tunneling microscopy (STM) (Fig. 3.12a). The self-assembly of aromatic carboxylic acids and cesium adatoms on Cu(100) substrate was studied by Stepanow<sup>129</sup> by means of STM and X-ray photoelectron spectroscopy. The well-ordered molecular nanostructures are built by the anionic carboxylate moieties and Cs cations, which produce the distinctive chirality of the network structures. A high flexibility of bond lengths and geometries result from the primary electrostatic interaction. Also the adsorbate substrate coupling plays an important role for the formation of the structures. With the use of rod-like carboxylic linker molecules, the dimension of the porous networks can be tuned by adjusting the aromatic backbone length (in Fig. 3.12b).

### 3. Results and discussions

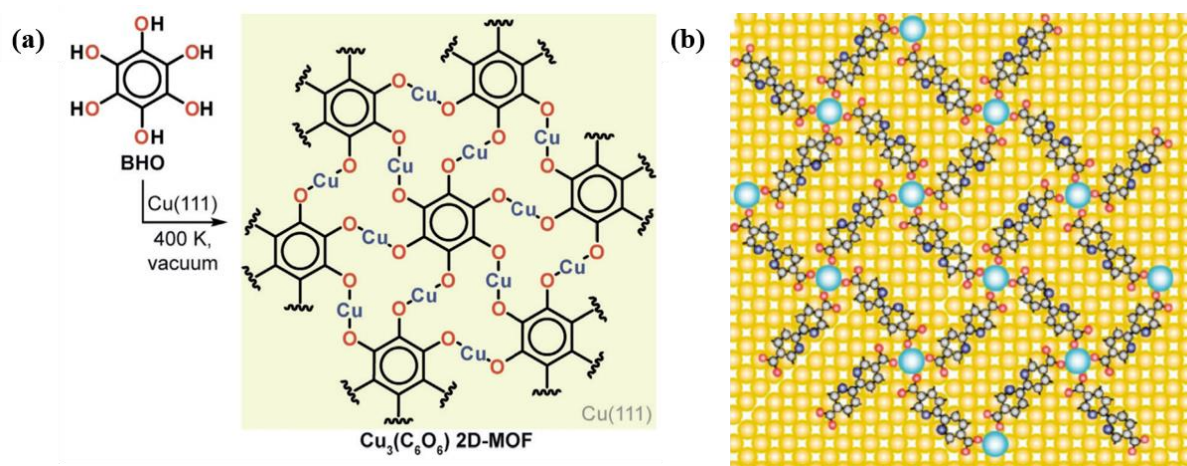


**Fig. 3.12: On-surface synthesis of 2D metal–organic framework (2D-MOF).** (a) On-surface synthesis of single layer of 2D-MOF  $\text{Cu}_3(\text{C}_6\text{O}_6)$ .<sup>128</sup>(b) An achiral network resulted from the organization of two chiral binding motifs alternatingly, which is indicated by a model.<sup>129</sup>

In our study,  $\text{PcZn}(\text{OH})_8$  molecules are deposited on an atomically flat  $\text{Ag}(111)$  single crystal surface by the homebuilt ES-CIBD under UHV conditions. Subsequently we use STM to visualize in real-space with submolecular resolution of the surface structures.

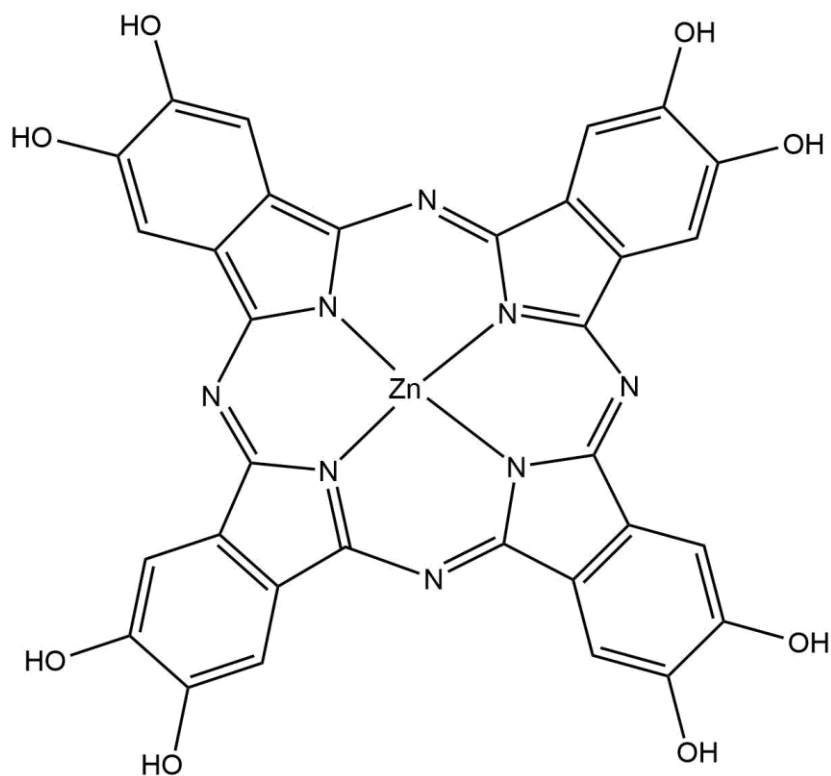
### 3.2.2 On-surface synthesis procedure

For the ES-CIBD, we used a solution of  $3.4 \times 10^{-3}$  M/L *PcZn(OH)<sub>8</sub>* molecules (Fig. 3.13, synthesized by the team of R. Dong & X. Feng, TU Dresden) in methanol. Gas-phase ions with +1 charge of the molecules were generated in the electrospray (voltage 3.5 kV on the emitter, flow rate 5-13  $\mu\text{l h}^{-1}$ , current up to  $\sim 100$  pA). Before the deposition in UHV, the composition of the ion beam was monitored by a digital quadrupole mass spectrometer and filtered by applying an additional DC offset. The deposition took place in a UHV chamber with a base pressure of  $9 \times 10^{-10}$  mbar and had a duration of 4.8 hours. The final amount of deposition of molecules is  $6.3 \times 10^{-12}$  mol. The landing energy of the molecular ion beam was 2.5 eV per charge to avoid fragmentation. Before the deposition, the Ag(111) single crystal was cleaned by repeated cycles of  $\text{Ar}^+$  sputtering and subsequent thermal annealing. The sputter gun can ionize argon and accelerate the argon ions with high voltage of 1 kV and emission current of 15 mA. The adsorbates and impurities are removed by bombarding the surface with  $\text{Ar}^+$ , but the top layers of the surface atoms are also partly removed, leaving a rough surface. The subsequent annealing in vacuum to 700 K can heal the surface and results in clean and atomically flat surfaces eventually. After the cleaning, the substrate was transferred to the deposition chamber. After dosing molecules, the sample was transferred to the STM chamber to do the analysis. STM measurements were conducted in a range between 110 K and 300 K. All voltages refer to the sample bias with respect to the tip. All STM measurements were performed with a chemically etched W tip. The STM data analysis was performed using WSxM.

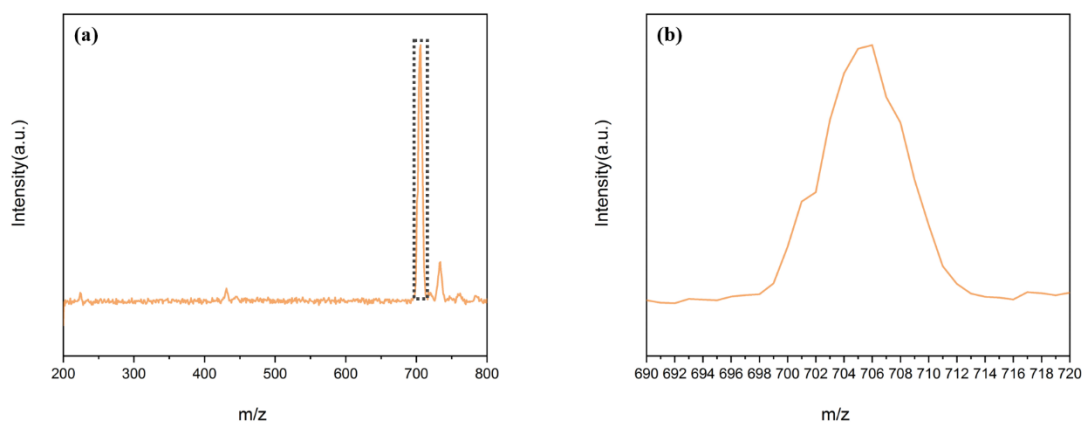
An important advantage of this approach is the possibility of extracting specific molecules from a mixture using the mass-filtered deposition capability of ES-CIBD. The  $m/z$  filtering quadrupole is initially tuned so that only the desired ions make their way to the substrate. STM imaging of the molecules deposited in this way reveals only structures corresponding to the selected molecules (Fig. 3.14a).

We studied the behavior of the molecules as a function of annealing temperature on metal surfaces Ag(111) after Fe deposition in UHV conditions.

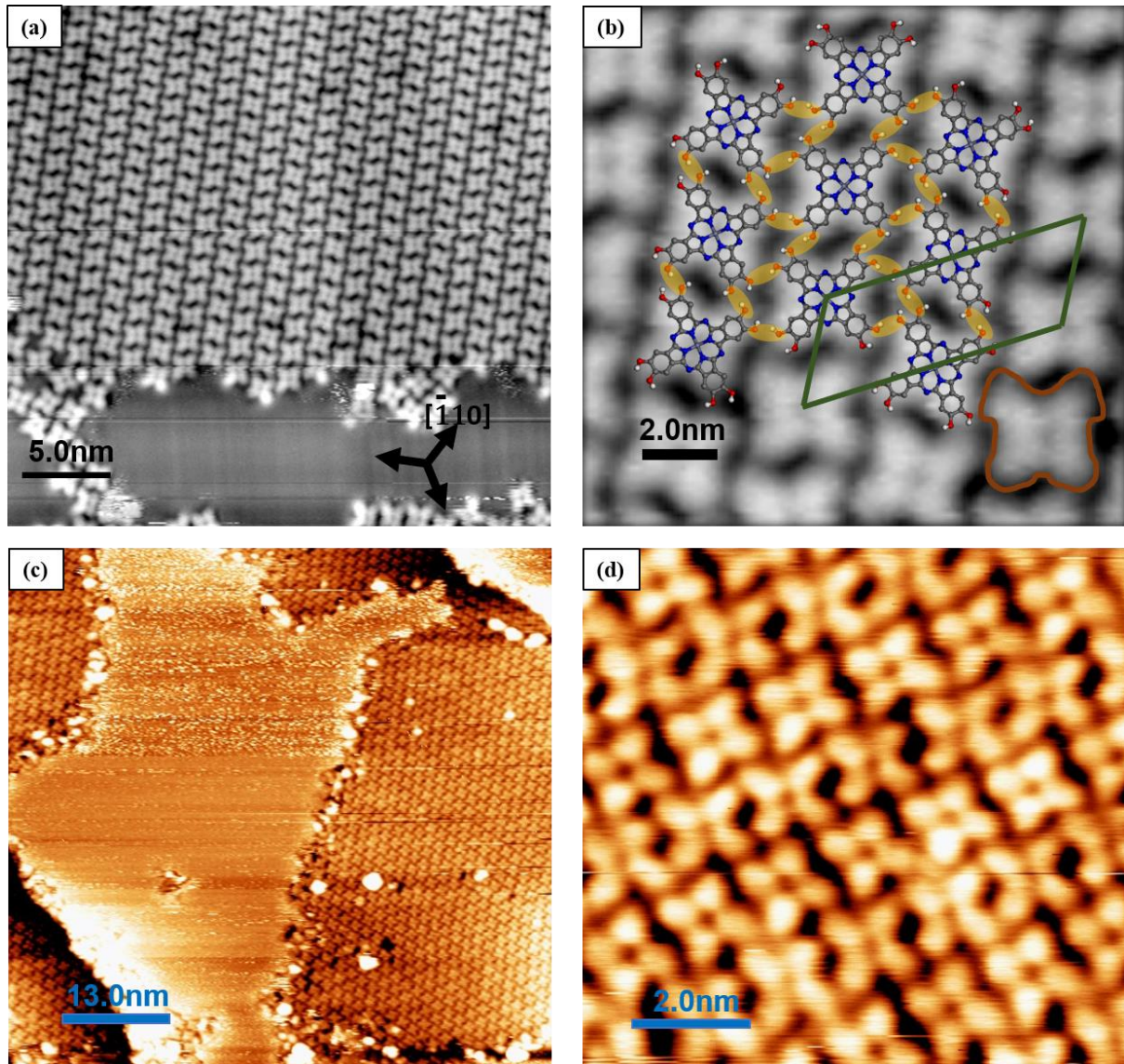
### 3. Results and discussions



**Fig. 3.13:** Chemical structure of PcZn(OH)<sub>8</sub> (C<sub>32</sub>H<sub>16</sub>N<sub>8</sub>O<sub>8</sub>Zn, molecular weight: 704 g/mol).



**Fig. 3.14:** (a) Mass spectrum of PcZn(OH)<sub>8</sub> in methanol. The selected m/z ratio for deposition is marked by the dashed rectangle. (b) Magnified mass spectrum of the area marked by a dotted rectangle in (a), assigned to PcZn(OH)<sub>8</sub>H<sup>+</sup>.

3.2.3 The self-assembly and metal adatom coordination of  $PcZn(OH)_8$  on  $Ag(111)$ 

**Fig. 3.15: Self-assembly of  $PcZn(OH)_8$  molecules deposited onto  $Ag(111)$  before and after dosing Fe.** (a) STM image of assembled molecules after deposition ( $T_{STM} \sim 113$  K,  $U_s = 2.2$  V,  $I_t = 0.12$  nA). The black bars indicate the high symmetry directions of the  $Ag(111)$  substrate. (b) Zoom in image of (a) showing a highly ordered molecular structure. ( $T_{STM} \sim 173$  K,  $U_s = 1.3$  V,  $I_t = 0.12$  nA), which is overlaid with corresponding ball-and-stick model. C, O, N, and H, Zn atoms are shown in black, red, blue, and white, light blue, respectively. The unit cell is indicated in green. The single molecule is outlined in orange. (c) STM image of assembled molecules after dosing of Fe. ( $T_{STM} \sim 300$  K,  $U_s = 1.5$  V,  $I_t = 0.06$  nA). (d) Magnified image showing the self-assembled structure. ( $T_{STM} \sim 300$  K,  $U_s = 0.5$  V,  $I_t = 0.06$  nA).

### 3. Results and discussions

Upon deposition on a Ag(111) substrate, which was held at RT,  $\text{PcZn(OH)}_8$  molecules formed close-packed molecular monolayer exhibiting a well-ordered molecular structure, which is shown in Fig. 3.15a. The molecule looks like four bright dots with one dark dot in the middle, which is outlined in orange. The  $\text{H}^+$ , added by the deposition process, likely stabilizes as  $\text{H}_{\text{ads}}$  on the surface before recombining to  $\text{H}_2$  and desorbing. Because we were unable to image the surface at RT, liquid nitrogen was employed to cool down the system for measurements. The angle between the orientation of assembly and  $\text{Ag}[\bar{1}10]$  direction is  $28^\circ$ . The molecules arrange in “zipper”-like structures. A zoom in image with a tentative model is shown in Fig. 3.15b, in which lateral intermolecular interactions consisting of hydrogen bonding  $\text{OH}\cdots\text{O}-\text{C}$ , indicated by yellow ovals, are at work to stabilize the self-assembly. In this circumstance, the unit cell has sides of 3.3 nm and 1.5 nm with an angle of  $65^\circ$  between them.

In order to investigate the coordination between the metal atoms and organic molecules, we dosed Fe after the deposition of the molecules. The measurements were conducted at RT, which indicates enhanced stability of the self-assembled structures resulting from the addition of Fe. Fig. 3.15c shows the assembly of the islands, with Fe clusters (visualized as white areas, due to the apparent height cut-off) found both at the edges and on top of the islands. The packing of the molecules after the dosing of Fe can be seen in Fig. 3.15d. The configuration shown in Fig. 3.15d is similar to Fig. 3.15b with rotated by  $60^\circ$  counterclockwise, which means the dosing of Fe has little influence on the interaction of molecules when the sample was held at RT.

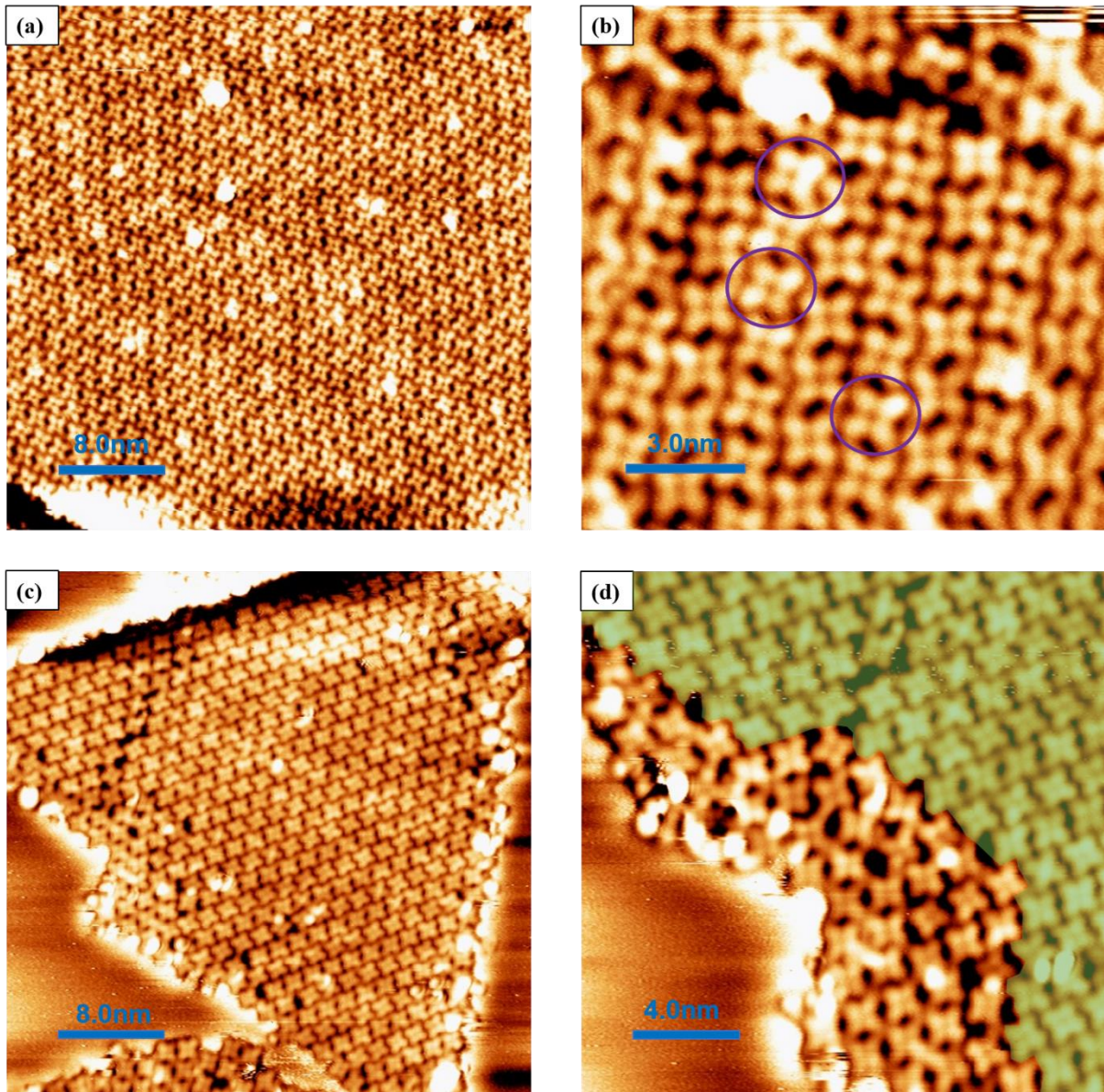


**Fig. 3.16: Fe coordination of  $\text{PcZn(OH)}_8$  on  $\text{Ag(111)}$  after annealing at 373 K.** (a) Large scale STM image of molecular island after annealing at 373 K. ( $T_{STM} \sim 300$  K,  $U_s = 1.8$  V,  $I_t = 0.11$  nA). (b) Zoom in image of (a) showing a less uniform molecular structure after the Fe deposition. Some “arms” of the molecules seem brighter or longer, which are indicated with purple circles ( $T_{STM} \sim 300$  K,  $U_s = 1.3$  V,  $I_t = 0.11$  nA). (c) STM image of assembled molecules of one island after annealing at 373K. ( $T_{STM} \sim 300$  K,  $U_s = 2.1$  V,  $I_t = 0.11$  nA). (d) Magnified image of (c) showing different molecular structure at the edge of the island. ( $T_{STM} \sim 300$  K,  $U_s = 2.1$  V,  $I_t = 0.11$  nA).

To investigate the coordination of the Fe atoms with the  $\text{PcZn(OH)}_8$  molecules on  $\text{Ag(111)}$ , we heated the sample at 373 K. Upon annealing the sample at 373 K, the sample was investigated by STM. The overview image Fig. 3.16a evidences the formation of a self-assembled close-packed two-dimensional phase. Fe clusters could be found on the surface of the assembled

### ***3. Results and discussions***

structure. Zoom in shows that the “zipper” structure is still be present in the islands. Moreover after the Fe deposition, some “arms” of the molecules seem brighter or longer, as indicated with purple circles, shown in Fig. 3.16b. This might hint to either an altered electronic structure due to Fe coordination or to the presence of an Fe atom in the vicinity. In Fig. 3.16c, two distinct phases associated with the presence of Fe on the surface are shown. The molecular packing in the center of the image comprises the majority of the structure, which is similar to the “zipper” structure observed in previous investigations. The molecular interactions can be rationalized based on a hydrogen bonding scheme as before. In Fig. 3.16d, the “zipper” phase was covered by yellow color. The phase at the edge of the island shows a different configuration compared to the phase in the center, as shown in Fig. 3.16d. The appearance of the “cross” structure is tentatively assigned to the molecules with coordination of Fe atoms. Clusters attributed to Fe could still be observed at the edge of the island.

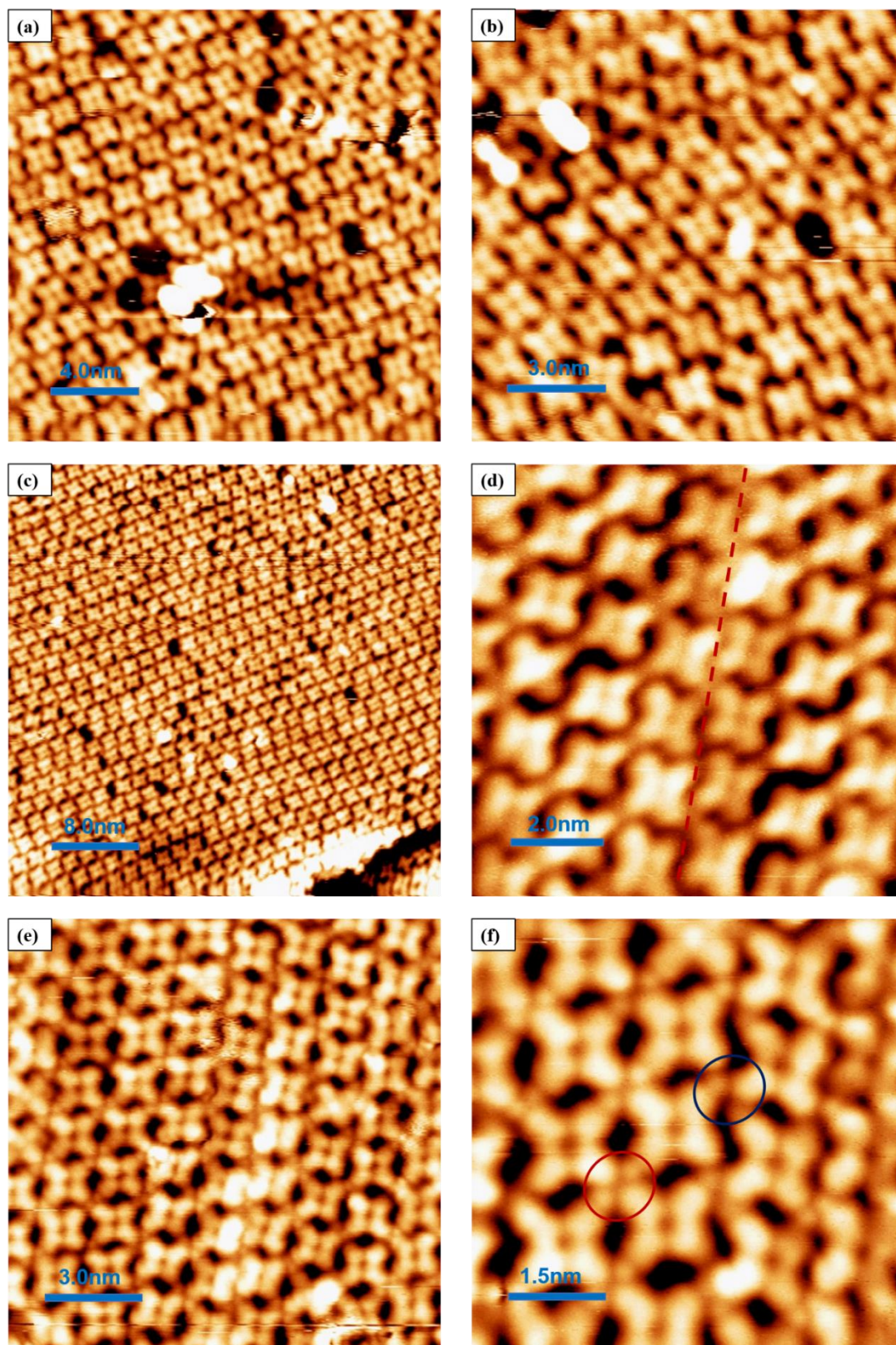


**Fig. 3.17:** Fe coordination of  $PcZn(OH)_8$  on  $Ag(111)$  after further annealing. (a) STM image of assembled molecules after annealing at 423 K for 30 min. ( $T_{STM} \sim 300$  K,  $U_s = 1.1$  V,  $I_t = 0.09$  nA). (b) Zoom in image of (a). ( $T_{STM} \sim 300$  K,  $U_s = 1.1$  V,  $I_t = 0.07$  nA). (c) Large scale STM image of assembled

### 3. Results and discussions

molecules after annealing at 423 K for 2 hours. ( $T_{STM} \sim 300$  K,  $U_s = 1.7$  V,  $I_t = 0.12$  nA). **(d)** Magnified image of (c), a molecular domain boundary is indicated with a dashed red line. ( $T_{STM} \sim 300$  K,  $U_s = 0.9$  V,  $I_t = 0.12$  nA). **(e)** STM image of assembled molecules after annealing at 448 K for 10 min. ( $T_{STM} \sim 300$  K,  $U_s = 0.8$  V,  $I_t = 0.12$  nA). **(f)** Magnified image of (e). Different Fe coordination nodes of the molecules are indicated with red and blue circles. ( $T_{STM} \sim 300$  K,  $U_s = 0.8$  V,  $I_t = 0.12$  nA).

Upon annealing the sample at 423 K for 30 min, the coordination structure can be observed by STM measurements (see Fig. 3.17a). The Fe coordination of the  $\text{PcZn(OH)}_8$  occurs at the center of the island. The zoom in image Fig. 3.17b shows that the zipper structure is still present. We therefore heat the sample at 423 K for another two hours. Afterwards, a more ordered network could be observed (Fig. 3.17c). Stacking faults in molecular domains appeared, as indicated with a dashed red line in Fig. 3.17d. To get a more coordinated structure, the sample was annealed to 448 K for 10 min. The Fe coordination of the molecules with higher order is shown in Fig. 3.17e. In a previous work, a metal-organic architecture on Cu(100) was investigated.<sup>130</sup> The node of carboxylic acids in their work is similar to the one shown in Fig. 3.17f, in which we can identify pairs of small round protrusions between molecular ligands, tentatively assigned to dimers of Fe atoms.

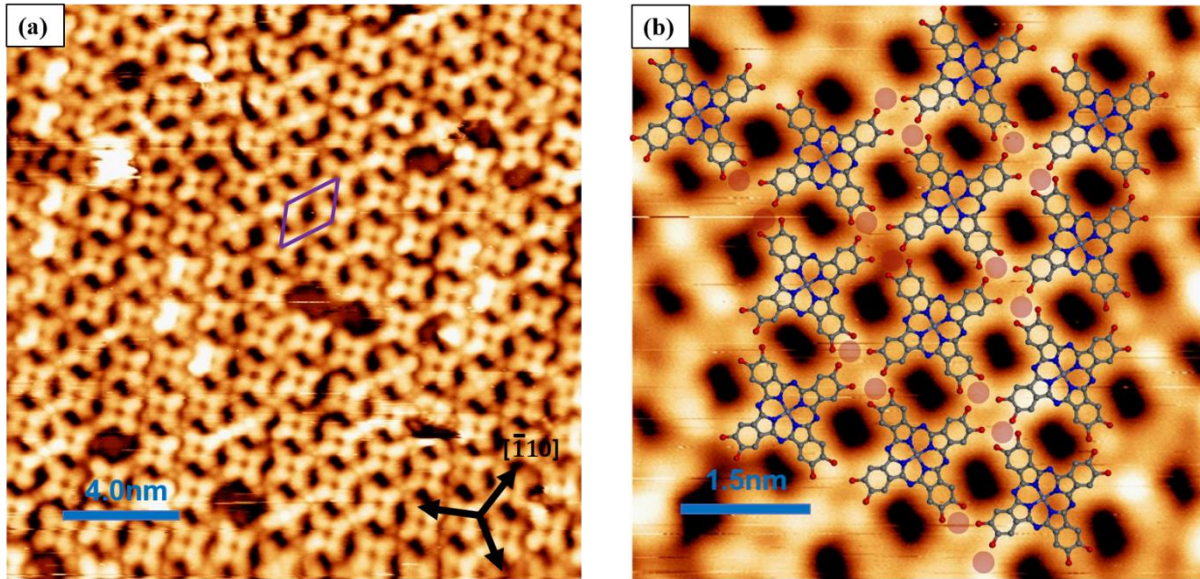


**Fig. 3.18: Fe coordination of  $PcZn(OH)_8$  on  $Ag(111)$  after annealing at 473 K.** (a) STM image of assembled molecules after annealing at 473 K. ( $T_{STM} \sim 300$  K,  $U_s = 1.1$  V,  $I_t = 0.07$  nA). The black bars indicate the high symmetry directions of the  $Ag(111)$  substrate. The unit cell is indicated in purple. (b) Magnification of (a) showing a detailed STM image overlaid with a model. The ball-and-stick model is based on the molecular structure. Red, dark blue, light blue and grey spheres represent oxygen, nitrogen, zinc and carbon, respectively. Light red spheres mark possible position of metal adatoms (Fe). ( $T_{STM} \sim 300$  K,  $U_s = -1.3$  V,  $I_t = -0.09$  nA).

To investigate the coordination motif further, we went to 473 K for the annealing. Large-scale STM image (Fig. 3.18a) shows a self-assembled molecular layer on the Ag surface after annealing. The unit cell has sides of 1.5 nm and 2.0 nm with an angle of  $55^\circ$  between them. The angles between the two sides and  $Ag[\bar{1}10]$  direction is  $29^\circ$  and  $26^\circ$ , respectively. Compared to the previous network at lower temperatures, the Fe coordination is more complete and Fe adatom dimers were tried to model the network nodes in Fig. 3.18b. The orientation of the molecules allows each molecule to coordinate to two adatoms (molecule: Fe= 1:2), in agreement with the STM image displayed in Fig. 3.18b. Urgel studied an interfacial 2D lanthanide-carboxylate network.<sup>131</sup> The bonding of ditopic linear linkers to Gd centers on  $Cu(111)$  comprises mononuclear nodes of eightfold lateral coordination. Aromatic carboxylic acids and cesium adatoms on a  $Cu(100)$  surface was investigated by Stepanow. The ratio of aromatic carboxylic acids to cesium adatoms is 2.<sup>132</sup>

### ***3. Results and discussions***

#### **3.2.4 Summary and conclusions**

A systematic study of the self-assembly  $\text{PcZn(OH)}_8$  molecules as well as their coordination with metal adatoms on closed packed coinage metal surface was presented. STM provides the atomic resolution topology of the architecture.  $\text{PcZn(OH)}_8$  molecules were investigated on Ag(111) to reveal its novel coordination motifs with metal atoms. We studied the influence of the annealing temperature on the nanoarchitectures.

## 3.3 The fabrication of microdevices based on GNRs

### 3.3.1 Introduction

Thanks to their unique physical properties, GNRs have been extensively investigated. They can be used in nano-electronics, spintronics, and optoelectronic devices with high performance.<sup>133–141</sup> Lately, quantum confinement and edge effects have been used to introduce a band gap in narrow graphene ribbons.<sup>133–136,138,142–144</sup> Thus, GNRs can be used to make field-effect transistors. In order to fabricate GNRs, some approaches have been developed, such as lithographic patterning,<sup>134,135</sup> chemical methods<sup>145</sup> and chemical sonication routes.<sup>142</sup>

A graphene nano-ribbon field-effect transistor device was fabricated via electron beam lithography and etching techniques by Chen<sup>135</sup> (Fig. 3.19a) and their electrical properties as a function of ribbon width were investigated too. Ribbons with a width range of 20, 30, 40, 50, 100 and 200 nm have been measured. The experimental results indicate that the resistivity of a ribbon increases as its width decreases under the impact of edge states. Besides, being different from CNTs with periodic boundary conditions being present, GNRs have edges with localized states<sup>133</sup> that can also have effects on the transport properties. Nano-scale chemically synthesized GNR field-effect transistors have been fabricated by a bottom-up method by Bennett *et al.* (Fig. 3.19b).<sup>79</sup> Then a layer transfer process was developed to fabricate three terminal transistor devices. By using e-beam lithography, a lot of source and drain contacts with nano-scale gaps of 100 nm widths were fabricated to measure the properties of the nanoribbons. A GNR-FET device with nanoribbons directly connected to bulk graphene electrodes was fabricated by Bai (Fig. 3.19c).<sup>146</sup> In their work, the graphene nanoribbons (GNRs) with sub-10 nm width were produced by using chemically synthesized nanowires as the physical protection mask in an oxygen plasma etching process. According to atomic force microscopy measurements, the resulting nanoribbons replicate exactly those of the mask nanowires down to 6 nm. They demonstrate that the results can be influenced by the GNR widths of the mask nanowire diameters with variable slopes and different etching times. Based on that, a GNR-FET device was fabricated and measured. In another study, CNTs were unzipped to produce GNRs by Ar plasma etching (Fig. 3.19d).<sup>147</sup> Multiwalled carbon nanotubes (MWCNTs) were embedded in a poly(methyl methacrylate) (PMMA) layer as an etching mask. Because the PMMA coating on the substrate is conformal, MWCNTs embedded in the PMMA film with a narrow strip not covered by PMMA was exposed to a Ar plasma. The unprotected side walls of MWCNTs were etched faster and removed by the plasma. After

### 3. Results and discussions

etching, the PMMA film was attached to a Si substrate with a 500-nm-thick layer of SiO<sub>2</sub>. Subsequently, it was removed by using acetone vapor and the polymer residue on the target substrate was removed by calcination. Afterwards three-terminal devices were fabricated with the GNRs with Pd as source and drain contacts.

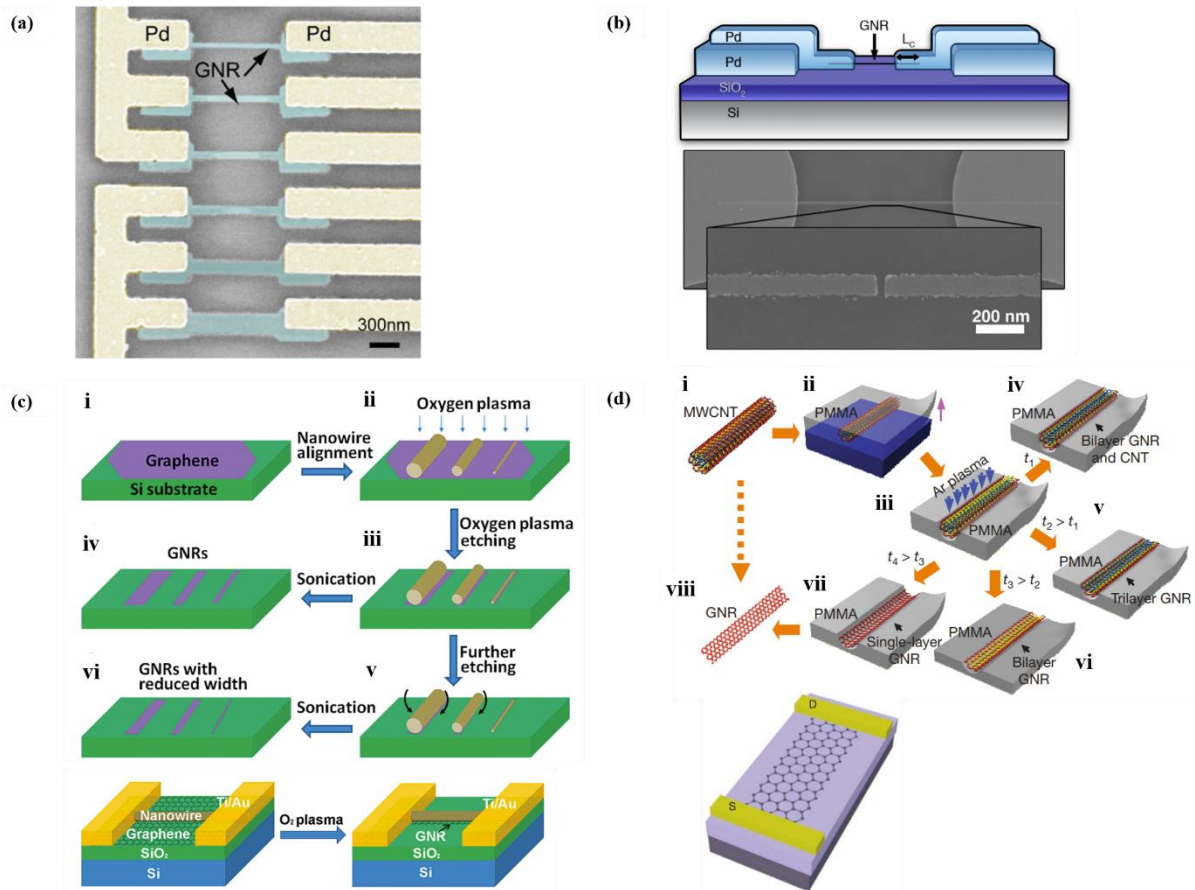


**Fig. 3.19: GNRs based electronics.** (a) SEM picture of GNR devices fabricated on a SiO<sub>2</sub> substrate. The widths of the GNRs from top to bottom are 20, 30, 40, 50, 100 and 200 nm respectively.<sup>135</sup> (b) Schematic illustrating device geometry. In order to obtain small channel lengths, Pd source and drain contacts have been fabricated by e-beam lithography.<sup>79</sup> (c) (i-vi) Schematic fabrication process of GNRs by means of oxygen plasma etching with a nanowire etch mask. Below, schematic illustration of the GNR-FET fabrication process.<sup>146</sup> (d) (i-viii) Schematic illustration of the procedure to make GNRs from CNTs. i, A pristine MWCNT was employed as the raw material. ii, The MWCNT was deposited on a Si substrate and afterwards coated with a PMMA film. iii, The PMMA–MWCNT film was peeled from the Si substrate, turned over and exposed to an Ar plasma. iv–vii, Several possible products were observed after etching for different times. viii, The PMMA was removed to obtain the GNR. Below it, schematic illustration of a GNR device. S represents source and D represents drain.<sup>147</sup>

### *3.3 The fabrication of microdevices based on GNRs*

In this study, we employed graphene nanoribbons with two different structures. The GNRs have an identical aromatic core but with alkyl side chains at different peripheral positions.<sup>148</sup> Based on theoretical modeling, the 6-CGNR-II, which features alkyl chains at the innermost positions, has a lower optical and electronic bandgaps by 0.2–0.3 eV, compared to the planar 6-CGNR-I substituted at the outermost positions because of 6-CGNR-II's structural distortion. Experimental ultraviolet-visible and near-infrared (UV-Vis-NIR) absorption and photoluminescence excitation (PLE) spectroscopy results of both planar 6-CGNR-I and nonplanar 6-CGNR-II are in agreement with the theoretical prediction. In order to investigate the potential difference of the electrical properties when 6-CGNR-I and 6-CGNR-II are used in devices, we fabricated GNR devices based on these material and report their transport characteristic by using optical lithography. In this work, diamond, C(100), was employed as the substrate since it is transparent, atomically flat and has a low resistivity.

### 3. Results and discussions

#### 3.3.2 Sample Preparation

To fabricate GNR devices, several processing procedures are necessary which consist of diamond cleaning, optical lithography, metallization and lift-off. The interdigitated and squared electrode fabrication process by means of top-down optical lithography is shown in Fig. 3.20.

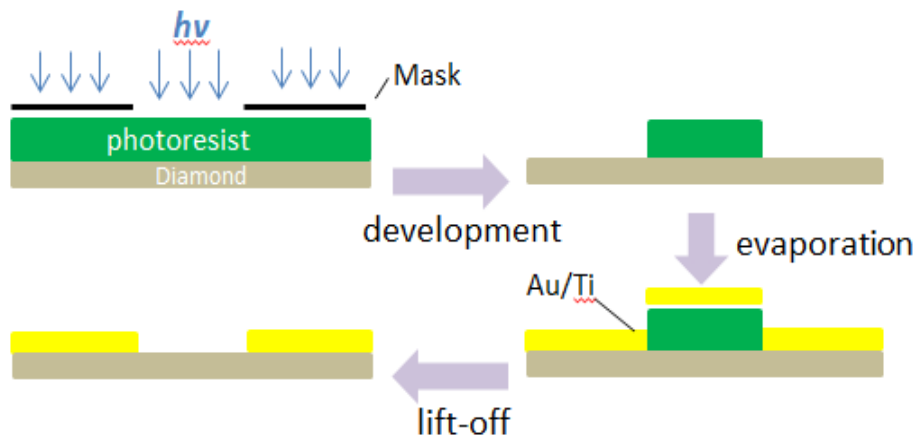


**Fig. 3.20: Processing steps for electrodes fabrication using an image reversal resist**

**1. Cleaning:** Diamond sheets with a flat surface were used as substrates. The surfaces were firstly cleaned with acetone, isopropanol and water in an ultrasonic bath, which is a standard cleaning process. The substrates were oxidized in oxygen plasma for 20 min. The resulting surface is shown in Fig. 3.21.

### 3.3 The fabrication of microdevices based on GNRs

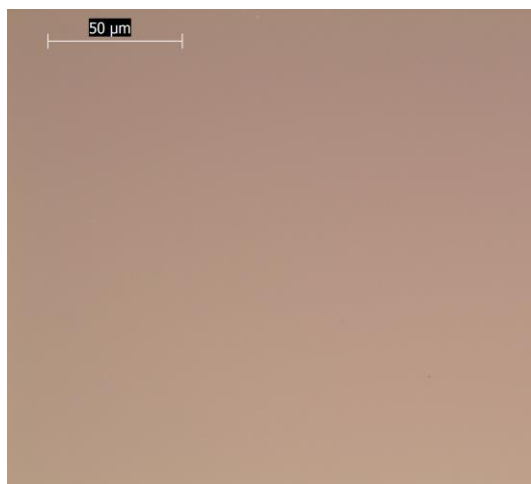


**Fig. 3.21: Optical microscope picture of diamond substrate after cleaning and plasma treatment**

**2. Drop-casting:** The 6-CGNR-I and 6-CGNR-II molecules (shown in Fig. 3.22, synthesized by the team of K. Müllen & A. Narita, Max Planck Institute for Polymer Research, Mainz, Germany) were dissolved in TCB (1,2,4-trichlorobenzene). The solutions of the molecules were deposited onto two diamond substrates surfaces by drop-casting (resulting surface shown in Fig. 3.23). These were dried overnight, followed by dipping in acetone for 10 seconds and dipping in isopropanol for 3 seconds (resulting surface shown in Fig. 3.24).

### 3. Results and discussions

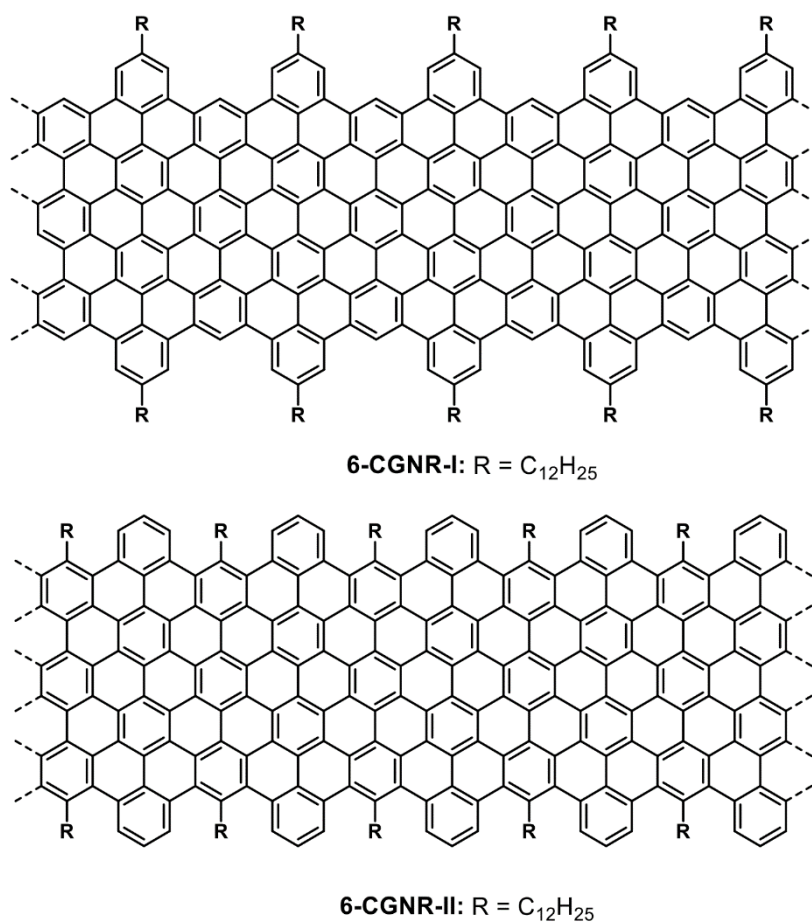


Fig. 3.22: Chemical structures of 6-CGNR-I and 6-CGNR-II.<sup>148</sup>

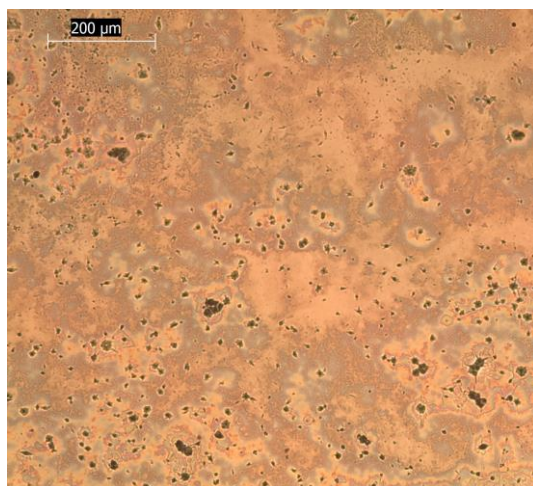
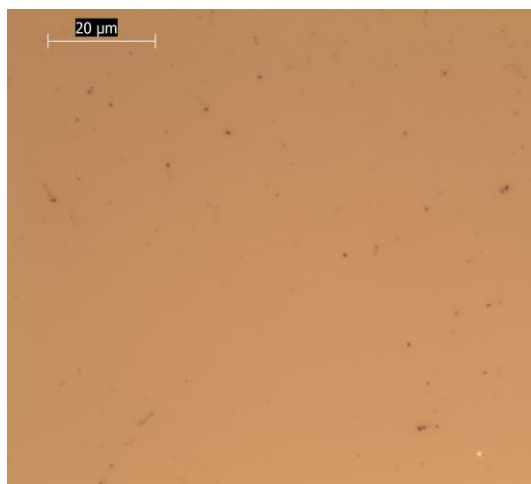


Fig. 3.23: Optical microscope picture of diamond substrate after drop-casting with a solution of 6-CGNR-I.

### 3.3 The fabrication of microdevices based on GNRs



**Fig. 3.24:** Optical microscope pictures of diamond after dipping in acetone for 10 seconds and dipping in isopropanol for 3 seconds respectively.

**3. Optical lithography:** The diamond substrates were afterwards spin-coated with a negative photoresist (AZ5214E) and baked at 110 °C for 1 min. The samples were exposed to UV light through a chromium lithographic mask in a 200 W mask aligner for 2 seconds (The mask aligner we used is a commercial product from SÜSS MicroTec). After the first exposure, the samples were baked in air at 120 °C for 2 min. Subsequently, the samples were exposed to UV light through a chromium lithographic mask in the mask aligner for 30 seconds. The unexposed parts of the resist were removed in a developing bath (AZ 400K Developer). We immersed the substrate into a standard developer solution, i.e. AZ 400K, 1 : 4 diluted, for 35 seconds. A part of the substrate's resist is removed, another part (that was exposed to a high temperature) remained (shown in Fig. 3.25). The photolithographic mask contains the pattern for electrodes of four different types. All of the patterns were square shaped but with different distances between them. The used distances were 2 μm, 4 μm, 6 μm, and 8 μm.

### 3. Results and discussions

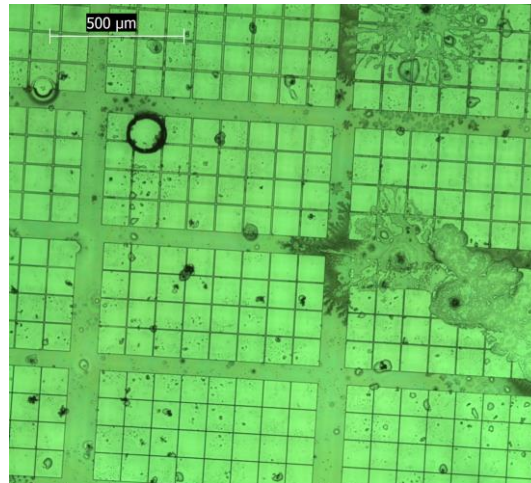


**Fig. 3.25: Optical microscope picture after development.**

**4. Metallization and lift-off:** A 10 nm titanium and 50 nm thick gold layer were deposited by means of electron beam evaporation (the evaporator we used is a commercial product from LEYBOLD AG). To remove the gold parts except for the electrodes, we have to lift-off the metal where it has photoresist underneath. To remove the photoresist, the sample was dipped into acetone and washed by an acetone flow with a strong flux with a plastic pipette for several minutes. The optical microscope was used to observe the electrodes after lift-off. After successful lift-off, the samples were cleaned again with acetone, rinsed with isopropyl alcohol as well as water and dried with nitrogen (result shown in Fig. 3.26).

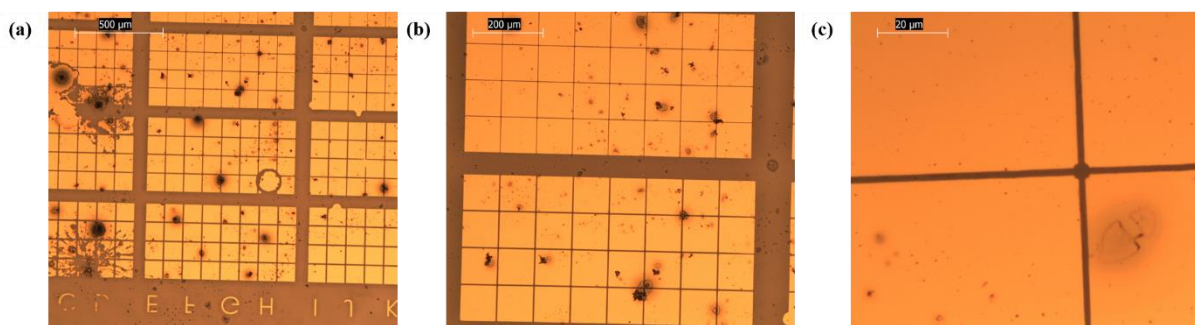


**Fig. 3.26: Optical microscope pictures of electrode pattern at different scales.**

**5. Electrical characterization of the devices:** The electrical measurement was carried out in air by using a probe station. (shown in Fig. 3.27)

### *3.3 The fabrication of microdevices based on GNRs*

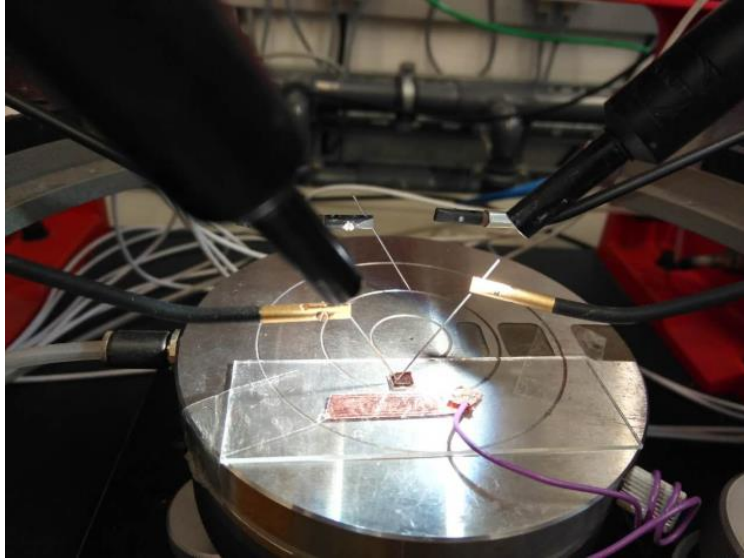


**Fig. 3.27: Electrical measurement of the GNR device on a probe station.**

### 3. Results and discussions

#### 3.3.3 Results and discussion

Growth of GNRs was previously reported via a chemical process.<sup>148</sup> 6-CGNR-I and 6-CGNR-II are exactly 7 carbon atoms across ( $n = 7$ ,  $w = 17.7 \text{ \AA}$ ) and have an estimated length of approximately 100 nm. Devices with patterned source drain gaps without any GNR did not show any conductance. Several devices with smaller gaps, such as  $2 \text{ }\mu\text{m}$ , exhibit semiconducting transport behavior with currents ranging from tens of nA to tens of  $\mu\text{A}$  at 1 V source drain bias. Because the ribbon orientation and position is random, the actual channel length and number of ribbons in each individual device is uncertain. For a gap distance is  $2 \text{ }\mu\text{m}$ , we estimate that in each device there are 0 to 20 GNRs long enough to potentially contact both the source and drain. Device yield is expected to increase significantly by further reducing the source-drain gap and/or increasing ribbon length during synthesis. Fig. 3.28 presents the electrical characterization of typical GNR devices measured in ambient conditions. Because of adsorbed oxygen, water, and residual resist resulting from optical lithography, such transistors exhibit large conductance variations. Due to the presence of a Schottky barrier at the metal-GNR interface, we used Ti/Au as the metal contact instead of Au. Nevertheless, the transport properties are still highly influenced by the Schottky junction contacts. 6-CGNR-I and 6-CGNR-II with different bandgaps<sup>148</sup> are supposed to show different transport characteristics. However according to the measurements presented in Fig. 3.28, the transport behavior of 6-CGNR-I and 6-CGNR-II are almost the same under the same conditions. Fig. 3.28 presents a transport characterization of typical devices made by 6-CGNR-I and 6-CGNR-II at 1 V, with  $2 \text{ }\mu\text{m}$  source-drain gap. The contact resistance between the GNRs and the Ti is depending on the GNR length and alignment. Despite this, we still see a large current, clearly demonstrating semiconducting transport in the GNRs. The observed device behavior is typical for a shortchannel Schottky barrier device.

### 3.3 The fabrication of microdevices based on GNRs

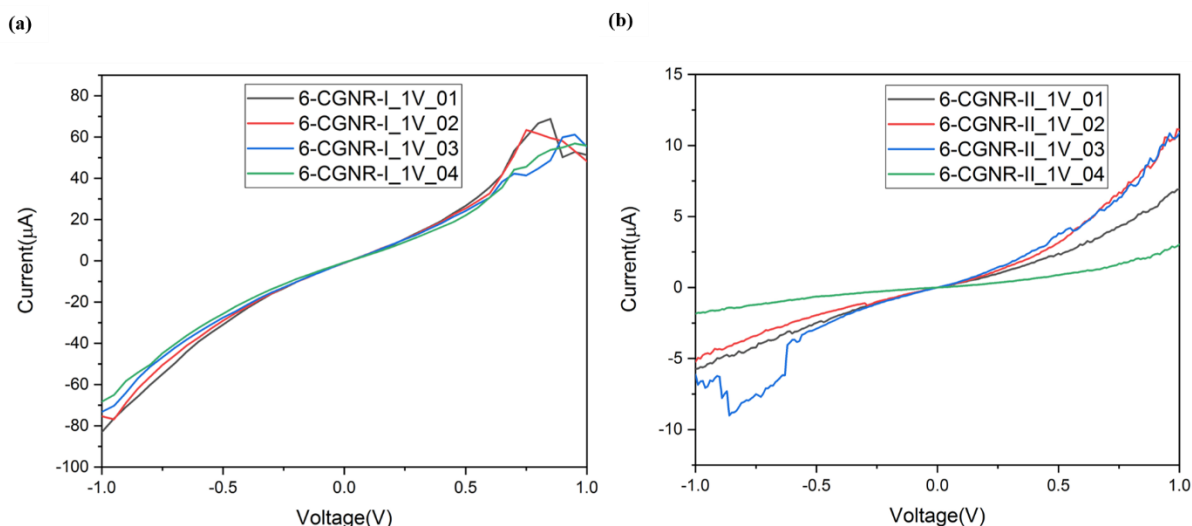


**Fig. 3.28:** (a) and (b) are showing the electrical characterization of typical devices based on 6-CGNR-I (a) and 6-CGNR-II (b) at 1 V source drain with a 2  $\mu\text{m}$  distance of source and drain.

Fig. 3.29 presents the electrical characterization of typical devices made by 6-CGNR-II measured in ambient conditions with a variable source drain gaps, which are 2,4,6,8  $\mu\text{m}$  respectively. As seen by the currents at different source-drain gap lengths shown in Fig. 3.29, the transport properties of the devices are obviously independent of the gaps lengths (within the range of 2  $\mu\text{m}$  to 8  $\mu\text{m}$ ). With the gap distance increasing, the current changes without following a trend. The main reason causing this could be the strategy of drop-casting employed in the fabrication process of the devices. Drop-casting a solution of GNR molecules on the diamond surface results in a very inhomogeneous distribution of molecules regarding the number of nanoribbons, their position as well as the orientation between the source and drain at different gap lengths. Thus, the transport properties shown in the measurements are nearly independent of the gap distances between the source and drain electrode.

### 3. Results and discussions

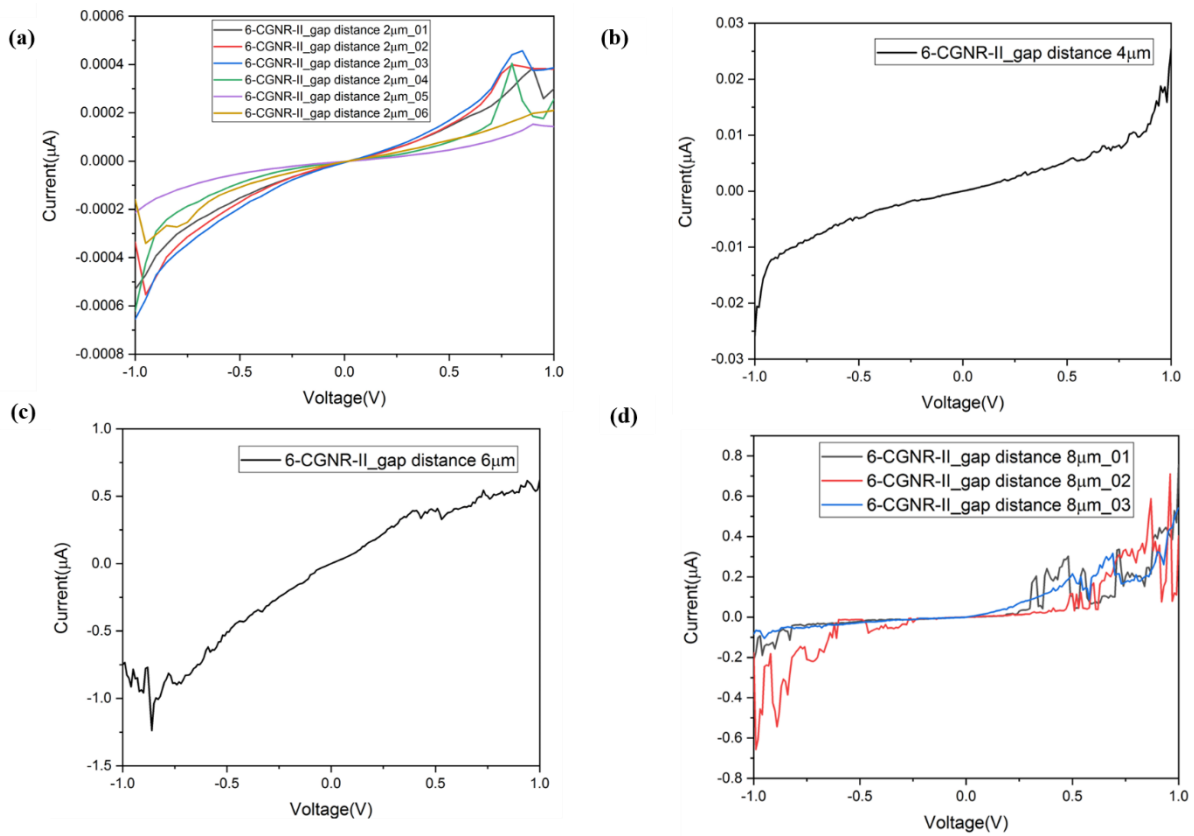


**Fig. 3.29:** (a) ,(b), (c) and (d) are showing electrical characterization of typical devices based on 6-CGNR-II at 1 V source drain bias with a 2,4,6,8  $\mu\text{m}$  source-drain gap respectively.

#### **3.3.4 Summary and conclusion**

The measurements shown previously indicate that the electronic properties of GNR devices are more significantly influenced by their environment such as adsorbed oxygen, water, and residual contamination resulting from optical lithography as well as the Schottky junction contacts as by the chemical structure of GNR with different edge modifications. The electronic behavior might be influenced by the local environment as well as edge modifications. In our study, the source-drain gaps seemed not to influence the electronic behavior of the GNR devices. Also, the exposure to air as well as the temperature could affect the results of the experiment.

By using drop casting, we could fabricate devices contacting chemically synthesized GNRs. With a probe station, the electronic transport of 6-CGNR-I and 6-CGNR-II devices have been investigated, which show a typical semiconducting transport behavior.

## 4. Conclusions

A systematic investigation of the self-assembly and polymerization of N-doped atomically-precise and homogenous graphene nanoribbons (NR10) synthesized in solution on close-packed atomically flat Ag(111) surfaces was presented in chapter 3.1 of this thesis. The deposition is accomplished by homebuilt ES-CIBD. The self-assembly and chemical reactions were resolved by means of STM. To investigate intermolecular interactions, the self-assembly at different coverages of NR10 molecules deposited onto an Ag(111) substrate held at RT was studied. On Ag(111), different self-assemblies were observed at different coverages. In order to study the chemical reactivity of NR10 on Ag(111) upon annealing, heating experiments at different temperatures were performed. After each annealing step, the sample was cooled back down for STM measurements. The Ag(111) surface was annealed to 423 K, 443 K, 483 K, 503 K, 523 K respectively. NR10 molecules heated to 423 K showed the same arrangement as after RT deposition. With the annealing temperatures going up, the self-assembly started to change. At the same time, cleavage of terminal groups and TIBS covegroups occurred. Subsequent annealing to 503 K leaves the molecules without any TIBS groups on the surface. To produce longer polymer chain instead of oligomers obtained at 523 K, we continued the annealing process. At annealing temperatures of 543 K, 563 K, 573 K and 583 K, individual 1D polymer chains could be observed. The distribution of different products of thermally induced reactions as a function of temperature was analyzed. To unravel the bond type of the polymer chain, we did a statistical analysis of the distances between two nearest bright protrusions within one monomer and of the distances between two nearest bright protrusions between two molecules in the polymer chain. The average distances between two nearest bright protrusions amount to 1.19 nm and 0.84 nm, respectively. 8 tentative models including metal-organic nodes were proposed for the connection nodes in the polymer chains. By comparing the distances between two nearest bright protrusions between the monomers within the polymer chains to the corresponding values of the proposed models, the nodes with 1 or 2 Ag within the polymer chain are found to be the best fitting ones, no matter whether they are assumed to be covalent

#### 4. Conclusions

bonds or coordination bonds. By careful inspection of the metal-organic nodes of the chain, the proposed models could be verified further. The next step of this project is to explore the chemical behavior on the metal surface of similar GNRs with larger length (NR20, NR30). As mentioned in chapter 3.3, the fabrication of GNRs devices can be considered as a preliminary step towards the fabrication of micro-devices based on NR10. It might be worthwhile to investigate the GNRs chain's polymerization on a substrate like diamond, which was used to fabricate micro-device based on 6-CGNR-I and 6-CGNR-II. After the polymerization on diamond in UHV, we could use the same approach as described in chapter 3.3 to fabricate GNR chain devices and characterize the electronic property as well as other physical properties. The work in chapter 3.3 relates well to the study of NR10 in chapter 3.1 and stimulates a continuation of the investigation.

Moreover, systematic study of the self-assembly  $\text{PcZn(OH)}_8$  molecules as well as their coordination with Fe adatoms on a closed packed coinage metal surface was presented in chapter 3.2. STM provides the atomic resolution topology of the architecture. Upon deposition using ES-CIBD on a Ag(111) substrate which was held at RT,  $\text{PcZn(OH)}_8$  molecules formed a close-packed molecular monolayer exhibiting a well-ordered molecular structure. In order to investigate the coordination between the metal atoms and the organic molecules, we dosed Fe after the deposition of molecules on the metallic surface. According to the results obtained from the STM images, the dosing of Fe has little influence on the interaction of molecules when the sample was held at RT. After annealing, the self-assembly changed and the coordination with Fe atoms was observed. When the sample was heated to 373 K, the "cross" structure starts to occur, which is tentatively assigned to molecules coordinating with Fe atoms. Upon annealing the sample to 423 K, a better ordered network could be observed. To promote more metal coordination within the structure, the sample was annealed to 448 K for 10 min. The Fe coordination of the molecules could be identified now by pairs of small round protrusions appearing in between molecular ligands in the STM images. These pairs can be tentatively assigned to dimers of Fe atoms. After heating to 473 K, the Fe coordination is more complete and Fe adatom dimers were considered as dominant network nodes. The next step of the work is to increase the coverage in order to create a second layer of molecules. Thus, a stack of 2D coordination networks might be built and studied.

## 5. Acknowledgements

Firstly, I would like to express a lot of thanks to Prof. Johannes Barth for giving me this opportunity to study at E20. Especially I want to thank him not only for his great supervision but also for his constant support during the whole period of time. He helped me in a lot of tough times and gave me courage and confidence. I also would like to thank Dr. Joachim Reichert for his supervision, discussions regarding to my work and he always encourages me to face the challenges and creates a very nice and relaxed working atmosphere. I am thankful to Dr. Anthoula Papageorgiou for her supervision and help with the analysis of the data. Both Dr. Joachim Reichert and Dr. Anthoula Papageorgiou are reachable if I need help. I would like to thank Dr. Hartmut Schlichting and Dr. Annette Huettig for their help in the lab and data analysis. I would like to thank the whole team of the STM-ESI group, to our team members Dr. Peter Knecht who gave me a very good introduction of STM and helped me with a lot of stuff, also to Dr. Andreas Walz, Dr. Karolina Stoiber and Hongxiang Xu for their scientific support, and helpful discussions as well as the nice working environment they created. I would like to express my sincere gratitude to Dr. Ignacio Piquero-Zulaica and Dr. Alexander Riss for their kind and unselfish help in my thesis writing. They gave me a lot of useful advices based on their experiences. Furthermore, I am very grateful to our secretary Viktoria Blaschek for her help and support in many aspects of my stay here. I would like to thank Karl Eberle and Reinhold Schneider for technical support and repairing a lot of lab equipment. Many thanks to Dr. Knud Seufert for his help in computer and software and thank Prof. Peter Feulner for his help in the lab and nice food he made. I especially want to thank my lunch group, Nan Cao, HongXiang Hu, Biao Yang, Yang Bao, Shengming Zhang, Wenchao Zhao, Kongchao Shen, Zhongliu Liu. The delightful discussions and the support they provide always gave me some relaxation. And of course I want to thank also everyone else at E20 for your kindness that makes me feel warmed. Finally, I am deeply grateful to my family for supporting me all the time during my study. You helped me in a lot of tough times and gave me confidence!

## References

- (1) Feynman, R. P. There's plenty of room at the bottom. California Institute of Technology, Engineering and Science magazine 1960.
- (2) Taniguchi, N.; Kohno, T.; Maruyama, K.; Iizuka, K.; Miyamoto, I.; Dohi, T. Nanotechnology: Integrated Processing Systems for Ultra-precision and Ultra-fine Products; Oxford University Press, 1996.
- (3) Arthur, J. R. Interaction of Ga and As<sub>2</sub> Molecular Beams with GaAs Surfaces. Journal of Applied Physics 1968, 39 (8), 4032–4034. DOI: 10.1063/1.1656901.
- (4) McCray, W. P. MBE deserves a place in the history books. Nat Nanotechnol 2007, 2 (5), 259–261. DOI: 10.1038/nnano.2007.121.
- (5) Suntola, T.; Antson, J. Method for producing compound thin films; Google Patents, 1977.
- (6) Wilbur, J. L.; Kumar, A.; Kim, E.; Whitesides, G. M. Microfabrication by microcontact printing of self-assembled monolayers. Adv. Mater. 1994, 6 (7–8), 600–604. DOI: 10.1002/adma.19940060719.
- (7) Delamarche, E. Microcontact Printing of Proteins; Wiley Online Books, 2004. DOI: 10.1002/3527602453.ch3.
- (8) Onclin, S.; Ravoo, B. J.; Reinhoudt, D. N. Engineering Silicon Oxide Surfaces Using Self-Assembled Monolayers. Angew. Chem. Int. Ed. 2005, 44 (39), 6282–6304. DOI: 10.1002/anie.200500633.
- (9) Perl, A.; Reinhoudt, D. N.; Huskens, J. Microcontact Printing: Limitations and Achievements. Adv. Mater. 2009, 21 (22), 2257–2268. DOI: 10.1002/adma.200801864.
- (10) Siringhaus, H.; Kawase, T.; Friend, R. H.; Shimoda, T.; Inbasekaran, M.; Wu, W.; Woo, E. P. High-Resolution Inkjet Printing of All-Polymer Transistor Circuits. Science 2000, 290 (5499), 2123. DOI: 10.1126/science.290.5499.212

## References

- (11) Li, Y.; Maynor, B. W.; Liu, J. Electrochemical AFM “Dip-Pen” Nanolithography. *Journal of the American Chemical Society* 2001, 123 (9), 2105–2106. DOI: 10.1021/ja005654m.
- (12) Salaita, K.; Wang, Y.; Mirkin, C. A. Applications of dip-pen nanolithography. *Nature Nanotechnology* 2007, 2 (3), 145–155. DOI: 10.1038/nnano.2007.39.
- (13) Liu, G.; Petrosko, S. H.; Zheng, Z.; Mirkin, C. A. Evolution of Dip-Pen Nanolithography (DPN): From Molecular Patterning to Materials Discovery. *Chemical Reviews* 2020, 120 (13), 6009–6047. DOI: 10.1021/acs.chemrev.9b00725.
- (14) Progress in digital integrated electronics; Maryland, USA, 1975.
- (15) Feyter, S. de; Uji-i, H.; Miura, A.; Mamdouh, W.; Zhang, J.; van Esch, J.; Feringa, B.; J. Schenning, A. P. H.; Meijer, E. W.; Wuerther, F.; Schryver, F. C. de. Supramolecular Chemistry at the Liquid/Solid Interface. *MRS Online Proceedings Library* 2006, 901 (1), 2001. DOI: 10.1557/PROC-0901-Ra20-01.
- (16) Keeling, D. L.; Oxtoby, N. S.; Wilson, C.; Humphry, M. J.; Champness, N. R.; Beton, P. H. Assembly and Processing of Hydrogen Bond Induced Supramolecular Nanostructures. *Nano Letters* 2003, 3 (1), 9–12. DOI: 10.1021/nl025821b.
- (17) Kudernac, T.; Lei, S.; Elemans, J. A.; Feyter, S. de. Two-dimensional supramolecular self-assembly: nanoporous networks on surfaces. *Chemical Society Reviews* 2009, 38 (2), 402–421.
- (18) Theobald, J. A.; Oxtoby, N. S.; Phillips, M. A.; Champness, N. R.; Beton, P. H. Controlling molecular deposition and layer structure with supramolecular surface assemblies. *Nature* 2003, 424 (6952), 1029–1031. DOI: 10.1038/nature01915.
- (19) Stepanow, S.; Lingenfelder, M.; Dmitriev, A.; Spillmann, H.; Delvigne, E.; Lin, N.; Deng, X.; Cai, C.; Barth, J. V.; Kern, K. Steering molecular organization and host–guest interactions using two-dimensional nanoporous coordination systems. *Nat Mater* 2004, 3 (4), 229–233. DOI: 10.1038/nmat1088.

- (20) van Hameren, R.; Schön, P.; van Buul, A. M.; Hoogboom, J.; Lazarenko, S. V.; Gerritsen, J. W.; Engelkamp, H.; Christianen, P. C. M.; Heus, H. A.; Maan, J. C. Macroscopic hierarchical surface patterning of porphyrin trimers via self-assembly and dewetting. *Science* 2006, 314 (5804), 1433–1436.
- (21) Furukawa, S.; Tahara, K.; Schryver, F. C. de; van der Auweraer, M.; Tobe, Y.; Feyter, S. de. Structural Transformation of a Two-Dimensional Molecular Network in Response to Selective Guest Inclusion. *Angew. Chem. Int. Ed.* 2007, 46 (16), 2831–2834. DOI: 10.1002/anie.200604782.
- (22) Pazos, E.; Novo, P.; Peinador, C.; Kaifer, A. E.; García, M. D. Cucurbit[8]uril (CB[8])-Based Supramolecular Switches. *Angew. Chem. Int. Ed.* 2019, 58 (2), 403–416. DOI: 10.1002/anie.201806575.
- (23) Chia, S.; Cao, J.; Stoddart, J. F.; Zink, J. I. Working Supramolecular Machines Trapped in Glass and Mounted on a Film Surface. *Angew. Chem. Int. Ed.* 2001, 40 (13), 2447–2451. DOI: 10.1002/1521-3773(20010702)40:13<2447:AID-ANIE2447>3.0.CO;2-P.
- (24) Cavallini, M.; Biscarini, F.; León, S.; Zerbetto, F.; Bottari, G.; Leigh, D. Information Storage Using Supramolecular Surface Patterns. *Science* 2003, 299, 531.
- (25) Decher, G.; Lehr, B.; Lowack, K.; Lvov, Y.; Schmitt, J. New nanocomposite films for biosensors: layer-by-layer adsorbed films of polyelectrolytes, proteins or DNA. *Biosensors and Bioelectronics* 1994, 9 (9), 677–684. DOI: 10.1016/0956-5663(94)80065-0.
- (26) Grill, L.; Dyer, M.; Lafferentz, L.; Persson, M.; Peters, M. V.; Hecht, S. Nano-architectures by covalent assembly of molecular building blocks. *Nature Nanotechnology* 2007, 2 (11), 687–691. DOI: 10.1038/nnano.2007.346.
- (27) Lackinger, M.; Heckl, W. M. A STM perspective on covalent intermolecular coupling reactions on surfaces. *Journal of Physics D: Applied Physics* 2011, 44 (46), 464011. DOI: 10.1088/0022-3727/44/46/464011.

## References

- (28) Perepichka, D. F.; Rosei, F. Extending Polymer Conjugation into the Second Dimension. *Science* 2009, 323 (5911), 216. DOI: 10.1126/science.1165429.
- (29) Narita, A.; Chen, Z.; Chen, Q.; Müllen, K. Solution and on-surface synthesis of structurally defined graphene nanoribbons as a new family of semiconductors. *Chemical Science* 2019, 10 (4), 964–975. DOI: 10.1039/C8SC03780A.
- (30) Björk, J. Reaction mechanisms for on-surface synthesis of covalent nanostructures. *Journal of Physics: Condensed Matter* 2016, 28 (8), 83002. DOI: 10.1088/0953-8984/28/8/083002.
- (31) Niu, T.; Zhang, J.; Chen, W. Atomic mechanism for the growth of wafer-scale single-crystal graphene: theoretical perspective and scanning tunneling microscopy investigations. *2D Materials* 2017, 4 (4), 42002. DOI: 10.1088/2053-1583/aa868f.
- (32) Weigelt, S.; Busse, C.; Bombis, C.; Knudsen, M. M.; Gothelf, K. V.; Strunskus, T.; Wöll, C.; Dahlbom, M.; Hammer, B.; Laegsgaard, E.; Besenbacher, F.; Linderöth, T. R. Covalent interlinking of an aldehyde and an amine on a Au(111) surface in ultrahigh vacuum. *Angew. Chem. Int. Ed.* 2007, 46 (48), 9227–9230. DOI: 10.1002/anie.200702859.
- (33) Weigelt, S.; Busse, C.; Bombis, C.; Knudsen, M. M.; Gothelf, K. V.; Lægsgaard, E.; Besenbacher, F.; Linderöth, T. R. Surface Synthesis of 2D Branched Polymer Nanostructures. *Angew. Chem. Int. Ed.* 2008, 47 (23), 4406–4410. DOI: 10.1002/anie.200705079.
- (34) Tanoue, R.; Higuchi, R.; Enoki, N.; Miyasato, Y.; Uemura, S.; Kimizuka, N.; Stieg, A. Z.; Gimzewski, J. K.; Kunitake, M. Thermodynamically Controlled Self-Assembly of Covalent Nanoarchitectures in Aqueous Solution. *ACS Nano* 2011, 5 (5), 3923–3929. DOI: 10.1021/nn200393q.
- (35) Tanoue, R.; Higuchi, R.; Ikebe, K.; Uemura, S.; Kimizuka, N.; Stieg, A. Z.; Gimzewski, J. K.; Kunitake, M. In Situ STM Investigation of Aromatic Poly(azomethine) Arrays Constructed by “On-Site” Equilibrium Polymerization. *Langmuir* 2012, 28 (39), 13844–13851. DOI: 10.1021/la302863h.

- (36) Liu, X.-H.; Guan, C.-Z.; Ding, S.-Y.; Wang, W.; Yan, H.-J.; Wang, D.; Wan, L.-J. On-Surface Synthesis of Single-Layered Two-Dimensional Covalent Organic Frameworks via Solid–Vapor Interface Reactions. *Journal of the American Chemical Society* 2013, 135 (28), 10470–10474. DOI: 10.1021/ja403464h.
- (37) Lafferentz, L.; Eberhardt, V.; Dri, C.; Africh, C.; Comelli, G.; Esch, F.; Hecht, S.; Grill, L. Controlling on-surface polymerization by hierarchical and substrate-directed growth. *Nature Chemistry* 2012, 4 (3), 215–220. DOI: 10.1038/nchem.1242.
- (38) Fan, Q.; Wang, C.; Han, Y.; Zhu, J.; Kuttner, J.; Hilt, G.; Gottfried, J. M. Surface-Assisted Formation, Assembly, and Dynamics of Planar Organometallic Macrocycles and Zigzag Shaped Polymer Chains with C–Cu–C Bonds. *ACS Nano* 2014, 8 (1), 709–718. DOI: 10.1021/nn405370s.
- (39) Gutzler, R.; Walch, H.; Eder, G.; Kloft, S.; Heckl, W. M.; Lackinger, M. Surface mediated synthesis of 2D covalent organic frameworks: 1,3,5-tris(4-bromophenyl)benzene on graphite(001), Cu(111), and Ag(110). *Chemical Communications* 2009 (29), 4456–4458. DOI: 10.1039/B906836H.
- (40) Bieri, M.; Treier, M.; Cai, J.; Aït-Mansour, K.; Ruffieux, P.; Gröning, O.; Gröning, P.; Kastler, M.; Rieger, R.; Feng, X.; Müllen, K.; Fasel, R. Porous graphenes: two-dimensional polymer synthesis with atomic precision. *Chemical Communications* 2009 (45), 6919–6921. DOI: 10.1039/B915190G.
- (41) Bieri, M.; Nguyen, M.-T.; Gröning, O.; Cai, J.; Treier, M.; Aït-Mansour, K.; Ruffieux, P.; Pignedoli, C. A.; Passerone, D.; Kastler, M.; Müllen, K.; Fasel, R. Two-Dimensional Polymer Formation on Surfaces: Insight into the Roles of Precursor Mobility and Reactivity. *Journal of the American Chemical Society* 2010, 132 (46), 16669–16676. DOI: 10.1021/ja107947z.
- (42) Blunt, M. O.; Russell, J. C.; Champness, N. R.; Beton, P. H. Templating molecular adsorption using a covalent organic framework. *Chemical Communications* 2010, 46 (38), 7157–7159. DOI: 10.1039/C0CC01810D.

## References

- (43) Rosei, F.; Schunack, M.; Naitoh, Y.; Jiang, P.; Gourdon, A.; Laegsgaard, E.; Stensgaard, I.; Joachim, C.; Besenbacher, F. Properties of large organic molecules on metal surfaces. *Progress in Surface Science* 2003, 71 (5-8), 95–146.
- (44) Barth, J. V.; Weckesser, J.; Cai, C.; Günter, P.; Bürgi, L.; Jeandupeux, O.; Kern, K. Building supramolecular nanostructures at surfaces by hydrogen bonding. *Angew. Chem. Int. Ed.* 2000, 39 (7), 1230–1234.
- (45) Barlow, S. M.; Raval, R. Complex organic molecules at metal surfaces: bonding, organisation and chirality. *Surface Science Reports* 2003, 50 (6-8), 201–341.
- (46) Wang, H.; Maiyalagan, T.; Wang, X. Review on recent progress in nitrogen-doped graphene: synthesis, characterization, and its potential applications. *Acs Catalysis* 2012, 2 (5), 781–794.
- (47) Zhao, L.; He, R.; Rim, K. T.; Schiros, T.; Kim, K. S.; Zhou, H.; Gutiérrez, C.; Chockalingam, S. P.; Arguello, C. J.; Pálová, L.; Nordlund, D.; Hybertsen, M. S.; Reichman, D. R.; Heinz, T. F.; Kim, P.; Pinczuk, A.; Flynn, G. W.; Pasupathy, A. N. Visualizing Individual Nitrogen Dopants in Monolayer Graphene. *Science* 2011, 333 (6045), 999. DOI: 10.1126/science.1208759.
- (48) Lv, R.; Li, Q.; Botello-Méndez, A. R.; Hayashi, T.; Wang, B.; Berkdemir, A.; Hao, Q.; Elías, A. L.; Cruz-Silva, R.; Gutiérrez, H. R.; Kim, Y. A.; Muramatsu, H.; Zhu, J.; Endo, M.; Terrones, H.; Charlier, J.-C.; Pan, M.; Terrones, M. Nitrogen-doped graphene: beyond single substitution and enhanced molecular sensing. *Sci Rep* 2012, 2, 586. DOI: 10.1038/srep00586.
- (49) Bronner, C.; Stremlau, S.; Gille, M.; Brauße, F.; Haase, A.; Hecht, S.; Tegeder, P. Aligning the Band Gap of Graphene Nanoribbons by Monomer Doping. *Angew. Chem. Int. Ed.* 2013, 52 (16), 4422–4425. DOI: 10.1002/anie.201209735.
- (50) Vo, T. H.; Shekhirev, M.; Kunkel, D. A.; Orange, F.; Guinel, M. J.-F.; Enders, A.; Sinitskii, A. Bottom-up solution synthesis of narrow nitrogen-doped graphene nanoribbons. *Chemical Communications* 2014, 50 (32), 4172–4174. DOI: 10.1039/C4CC00885E.

(51) Cai, J.; Pignedoli, C. A.; Talirz, L.; Ruffieux, P.; Söde, H.; Liang, L.; Meunier, V.; Berger, R.; Li, R.; Feng, X.; Müllen, K.; Fasel, R. Graphene nanoribbon heterojunctions. *Nature Nanotechnology* 2014, 9 (11), 896–900. DOI: 10.1038/nnano.2014.184.

(52) Wang, X.; Li, X.; Zhang, L.; Yoon, Y.; Weber, P. K.; Wang, H.; Guo, J.; Dai, H. N-Doping of Graphene Through Electrothermal Reactions with Ammonia. *Science* 2009, 324 (5928), 768. DOI: 10.1126/science.1170335.

(53) Liu, X.; Zhang, X. W.; Meng, J. H.; Yin, Z. G.; Zhang, L. Q.; Wang, H. L.; Wu, J. L. High efficiency Schottky junction solar cells by co-doping of graphene with gold nanoparticles and nitric acid. *Applied Physics Letters* 2015, 106 (23), 233901. DOI: 10.1063/1.4922373.

(54) Qu, L.; Liu, Y.; Baek, J.-B.; Dai, L. Nitrogen-doped graphene as efficient metal-free electrocatalyst for oxygen reduction in fuel cells. *ACS Nano* 2010, 4 (3), 1321–1326.

(55) Elías, A. L.; Carrero-Sánchez, J. C.; Terrones, H.; Endo, M.; Laclette, J. P.; Terrones, M. Viability studies of pure carbon- and nitrogen-doped nanotubes with *Entamoeba histolytica*: from amoebicidal to biocompatible structures. *Small* 2007, 3 (10), 1723–1729.

(56) Carrero-Sánchez, J. C.; Elías, A. L.; Mancilla, R.; Arrellín, G.; Terrones, H.; Laclette, J. P.; Terrones, M. Biocompatibility and Toxicological Studies of Carbon Nanotubes Doped with Nitrogen. *Nano Letters* 2006, 6 (8), 1609–1616. DOI: 10.1021/nl060548p.

(57) Wang, Y.; Shao, Y.; Matson, D. W.; Li, J.; Lin, Y. Nitrogen-Doped Graphene and Its Application in Electrochemical Biosensing. *ACS Nano* 2010, 4 (4), 1790–1798. DOI: 10.1021/nn100315s.

(58) Binnig, G.; Rohrer, H.; Gerber, C.; Weibel, E. Surface Studies by Scanning Tunneling Microscopy. *Phys. Rev. Lett.* 1982, 49 (1), 57–61. DOI: 10.1103/PhysRevLett.49.57.

(59) Atkins, P. W.; Paula, J. de. *Physikalische chemie*; John Wiley & Sons, 2013.

## *References*

- (60) Engel, A. Introduction to scanning tunneling microscopy By C. Julian Chen Oxford University Press, New York (1993) ISBN 0-19-507150-6; \$65.00. Scanning 1994, 16 (2), 123–124. DOI: 10.1002/sca.4950160210.
- (61) Bardeen, J. Tunnelling from a many-particle point of view. Phys. Rev. Lett. 1961, 6 (2), 57.
- (62) Tersoff, J.; Hamann, D. R. Theory of the scanning tunneling microscope. Phys. Rev. B 1985, 31 (2), 805.
- (63) Marturi, N. Vision and visual servoing for nanomanipulation and nanocharacterization in scanning electron microscope 2013.
- (64) Mironov, V. Fundamentals of Scanning Probe Microscopy, 2014.
- (65) Besenbacher, F.; Lægsgaard, E.; Stensgaard, I. Fast-scanning STM studies. Materials Today 2005, 8 (5), 26–30.
- (66) Laegsgaard, E.; Österlund, L.; Thostrup, P.; Rasmussen, P. B.; Stensgaard, I.; Besenbacher, F. A high-pressure scanning tunneling microscope. Review of Scientific Instruments 2001, 72 (9), 3537–3542. DOI: 10.1063/1.1389497.
- (67) Jiang, L. Chemistry on noble metal surfaces: Towards covalently linked nanoarchitectures, Technische Universität München, 2017.
- (68) McEwen, C. N.; Larsen, B. S. Fifty years of desorption ionization of nonvolatile compounds. International Journal of Mass Spectrometry 2015, 377, 515–531. DOI: 10.1016/j.ijms.2014.07.018.
- (69) Vestal, M. L. Methods of Ion Generation. Chemical Reviews 2001, 101 (2), 361–376. DOI: 10.1021/cr990104w.
- (70) Monge, M. E.; Harris, G. A.; Dwivedi, P.; Fernández, F. M. Mass Spectrometry: Recent Advances in Direct Open Air Surface Sampling/Ionization. Chemical Reviews 2013, 113 (4), 2269–2308. DOI: 10.1021/cr300309q.

- (71) Fenn, J. B. Electrospray Wings for Molecular Elephants (Nobel Lecture). *Angew. Chem. Int. Ed.* 2003, 42 (33), 3871–3894. DOI: 10.1002/anie.200300605.
- (72) Fenn, J. B.; Mann, M.; Meng, C. K.; Wong, S. F.; Whitehouse, C. M. Electrospray ionization for mass spectrometry of large biomolecules. *Science* 1989, 246 (4926), 64. DOI: 10.1126/science.2675315.
- (73) Siuzdak, G.; Bothner, B.; Yeager, M.; Brugidou, C.; Fauquet, C. M.; Hoey, K.; Change, C.-M. Mass spectrometry and viral analysis. *Chemistry & Biology* 1996, 3 (1), 45–48. DOI: 10.1016/S1074-5521(96)90083-6.
- (74) Wilm, M. Principles of Electrospray Ionization. *Molecular & Cellular Proteomics* 2011, 10 (7), M111.009407. DOI: 10.1074/mcp.M111.009407.
- (75) Rauschenbach, S.; Ternes, M.; Harnau, L.; Kern, K. Mass Spectrometry as a Preparative Tool for the Surface Science of Large Molecules. *Annual Review of Analytical Chemistry* 2016, 9 (1), 473–498. DOI: 10.1146/annurev-anchem-071015-041633.
- (76) Verbeck, G.; Hoffmann, W.; Walton, B. Soft-landing preparative mass spectrometry. *Analyst* 2012, 137 (19), 4393–4407. DOI: 10.1039/C2AN35550G.
- (77) Taylor, G. I. Disintegration of water drops in an electric field. *Proceedings of the Royal Society of London. Series A. Mathematical and Physical Sciences* 1964, 280 (1382), 383–397. DOI: 10.1098/rspa.1964.0151.
- (78) Kaposi, T.; Barth, J.; Heiz, U. K. A Compact and Versatile Electrospray Ion Beam Deposition Setup Advanced Sample Preparation for Experiments in Surface Science. <https://nbn-resolving.org/urn:nbn:de:bvb:91-diss-20160531-1292664-1-3>.
- (79) Patrick B. Bennett; Zahra Pedramrazi; Ali Madani; Yen-Chia Chen; Dimas G. de Oteyza; Chen Chen; Felix R. Fischer; Michael F. Crommie; Jeffrey Bokor. Bottom-up graphene nanoribbon field-effect transistors. *Applied Physics Letters* 2013, 103 (25), 253114. DOI: 10.1063/1.4855116.
- (80) Llinas, J. P.; Fairbrother, A.; Borin Barin, G.; Shi, W.; Lee, K.; Wu, S.; Yong Choi, B.; Braganza, R.; Lear, J.; Kau, N.; Choi, W.; Chen, C.; Pedramrazi, Z.; Dumslaff, T.; Narita, A.;

## References

- Feng, X.; Müllen, K.; Fischer, F.; Zettl, A.; Ruffieux, P.; Yablonovitch, E.; Crommie, M.; Fasel, R.; Bokor, J. Short-channel field-effect transistors with 9-atom and 13-atom wide graphene nanoribbons. *Nature Communications* 2017, 8 (1), 633. DOI: 10.1038/s41467-017-00734-x.
- (81) Passi, V.; Gahoi, A.; Senkovskiy, B. V.; Haberer, D.; Fischer, F. R.; Grüneis, A.; Lemme, M. C. Field-Effect Transistors Based on Networks of Highly Aligned, Chemically Synthesized N = 7 Armchair Graphene Nanoribbons. *ACS Applied Materials & Interfaces* 2018, 10 (12), 9900–9903. DOI: 10.1021/acsami.8b01116.
- (82) A. Kargar; C. Lee. Graphene nanoribbon schottky diodes using asymmetric contacts. In 2009 9th IEEE Conference on Nanotechnology (IEEE-NANO), 2009; pp 243–245.
- (83) A. Naeemi; J. D. Meindl. Conductance Modeling for Graphene Nanoribbon (GNR) Interconnects. *IEEE Electron Device Letters* 2007, 28 (5), 428–431. DOI: 10.1109/LED.2007.895452.
- (84) Cai, J.; Ruffieux, P.; Jaafar, R.; Bieri, M.; Braun, T.; Blankenburg, S.; Muoth, M.; Seitsonen, A. P.; Saleh, M.; Feng, X.; Müllen, K.; Fasel, R. Atomically precise bottom-up fabrication of graphene nanoribbons. *Nature* 2010, 466 (7305), 470–473. DOI: 10.1038/nature09211.
- (85) Talirz, L.; Ruffieux, P.; Fasel, R. On-Surface Synthesis of Atomically Precise Graphene Nanoribbons. *Adv. Mater.* 2016, 28 (29), 6222–6231. DOI: 10.1002/adma.201505738.
- (86) Ruffieux, P.; Wang, S.; Yang, B.; Sánchez-Sánchez, C.; Liu, J.; Dienel, T.; Talirz, L.; Shinde, P.; Pignedoli, C. A.; Passerone, D.; Dumslaff, T.; Feng, X.; Müllen, K.; Fasel, R. On-surface synthesis of graphene nanoribbons with zigzag edge topology. *Nature* 2016, 531 (7595), 489–492. DOI: 10.1038/nature17151.
- (87) Oteyza, D. G. de; García-Lekue, A.; Vilas-Varela, M.; Merino-Díez, N.; Carbonell-Sanromà, E.; Corso, M.; Vasseur, G.; Rogero, C.; Guitián, E.; Pascual, J. I.; Ortega, J. E.; Wakayama, Y.; Peña, D. Substrate-Independent Growth of Atomically Precise Chiral Graphene Nanoribbons. *ACS Nano* 2016, 10 (9), 9000–9008. DOI: 10.1021/acsnano.6b05269.

(88) Merino-Díez, N.; Garcia-Lekue, A.; Carbonell-Sanromà, E.; Li, J.; Corso, M.; Colazzo, L.; Sedona, F.; Sánchez-Portal, D.; Pascual, J. I.; Oteyza, D. G. de. Width-Dependent Band Gap in Armchair Graphene Nanoribbons Reveals Fermi Level Pinning on Au(111). *ACS Nano* 2017, 11 (11), 11661–11668. DOI: 10.1021/acsnano.7b06765.

(89) Chen, Y.-C.; Oteyza, D. G. de; Pedramrazi, Z.; Chen, C.; Fischer, F. R.; Crommie, M. F. Tuning the Band Gap of Graphene Nanoribbons Synthesized from Molecular Precursors. *ACS Nano* 2013, 7 (7), 6123–6128. DOI: 10.1021/nn401948e.

(90) Abdurakhmanova, N.; Amsharov, N.; Stepanow, S.; Jansen, M.; Kern, K.; Amsharov, K. Synthesis of wide atomically precise graphene nanoribbons from para-oligophenylene based molecular precursor. *Carbon* 2014, 77, 1187–1190. DOI: 10.1016/j.carbon.2014.06.010.

(91) Kimouche, A.; Ervasti, M. M.; Drost, R.; Halonen, S.; Harju, A.; Joensuu, P. M.; Sainio, J.; Liljeroth, P. Ultra-narrow metallic armchair graphene nanoribbons. *Nature Communications* 2015, 6 (1), 10177. DOI: 10.1038/ncomms10177.

(92) Zhang, H.; Lin, H.; Sun, K.; Chen, L.; Zagranyski, Y.; Aghdassi, N.; Duhm, S.; Li, Q.; Zhong, D.; Li, Y.; Müllen, K.; Fuchs, H.; Chi, L. On-Surface Synthesis of Rylene-Type Graphene Nanoribbons. *Journal of the American Chemical Society* 2015, 137 (12), 4022–4025. DOI: 10.1021/ja511995r.

(93) Talirz, L.; Söde, H.; Dumslaff, T.; Wang, S.; Sanchez-Valencia, J. R.; Liu, J.; Shinde, P.; Pignedoli, C. A.; Liang, L.; Meunier, V.; Plumb, N. C.; Shi, M.; Feng, X.; Narita, A.; Müllen, K.; Fasel, R.; Ruffieux, P. On-Surface Synthesis and Characterization of 9-Atom Wide Armchair Graphene Nanoribbons. *ACS Nano* 2017, 11 (2), 1380–1388. DOI: 10.1021/acsnano.6b06405.

(94) Cloke, R. R.; Marangoni, T.; Nguyen, G. D.; Joshi, T.; Rizzo, D. J.; Bronner, C.; Cao, T.; Louie, S. G.; Crommie, M. F.; Fischer, F. R. Site-Specific Substitutional Boron Doping of Semiconducting Armchair Graphene Nanoribbons. *Journal of the American Chemical Society* 2015, 137 (28), 8872–8875. DOI: 10.1021/jacs.5b02523.

## References

- (95) Kawai, S.; Nakatsuka, S.; Hatakeyama, T.; Pawlak, R.; Meier, T.; Tracey, J.; Meyer, E.; Foster, A. S. Multiple heteroatom substitution to graphene nanoribbon. *Science Advances* 2018, 4 (4), eaar7181. DOI: 10.1126/sciadv.aar7181.
- (96) Nguyen, G. D.; Toma, F. M.; Cao, T.; Pedramrazi, Z.; Chen, C.; Rizzo, D. J.; Joshi, T.; Bronner, C.; Chen, Y.-C.; Favaro, M.; Louie, S. G.; Fischer, F. R.; Crommie, M. F. Bottom-Up Synthesis of N = 13 Sulfur-Doped Graphene Nanoribbons. *The Journal of Physical Chemistry C* 2016, 120 (5), 2684–2687. DOI: 10.1021/acs.jpcc.5b09986.
- (97) Wang, X.-Y.; Urgel, J. I.; Barin, G. B.; Eimre, K.; Di Giovannantonio, M.; Milani, A.; Tommasini, M.; Pignedoli, C. A.; Ruffieux, P.; Feng, X.; Fasel, R.; Müllen, K.; Narita, A. Bottom-Up Synthesis of Heteroatom-Doped Chiral Graphene Nanoribbons. *Journal of the American Chemical Society* 2018, 140 (29), 9104–9107. DOI: 10.1021/jacs.8b06210.
- (98) Durr, R. A.; Haberer, D.; Lee, Y.-L.; Blackwell, R.; Kalayjian, A. M.; Marangoni, T.; Ihm, J.; Louie, S. G.; Fischer, F. R. Orbitally Matched Edge-Doping in Graphene Nanoribbons. *Journal of the American Chemical Society* 2018, 140 (2), 807–813. DOI: 10.1021/jacs.7b11886.
- (99) Carbonell-Sanromà, E.; Hieulle, J.; Vilas-Varela, M.; Brandimarte, P.; Iraola, M.; Barragán, A.; Li, J.; Abadia, M.; Corso, M.; Sánchez-Portal, D.; Peña, D.; Pascual, J. I. Doping of Graphene Nanoribbons via Functional Group Edge Modification. *ACS Nano* 2017, 11 (7), 7355–7361. DOI: 10.1021/acsnano.7b03522.
- (100) Nguyen, G. D.; Tsai, H.-Z.; Omrani, A. A.; Marangoni, T.; Wu, M.; Rizzo, D. J.; Rodgers, G. F.; Cloke, R. R.; Durr, R. A.; Sakai, Y.; Liou, F.; Aikawa, A. S.; Chelikowsky, J. R.; Louie, S. G.; Fischer, F. R.; Crommie, M. F. Atomically precise graphene nanoribbon heterojunctions from a single molecular precursor. *Nature Nanotechnology* 2017, 12 (11), 1077–1082. DOI: 10.1038/nnano.2017.155.
- (101) Wang, W.; Shi, X.; Wang, S.; van Hove, M. A.; Lin, N. Single-Molecule Resolution of an Organometallic Intermediate in a Surface-Supported Ullmann Coupling Reaction. *Journal of the American Chemical Society* 2011, 133 (34), 13264–13267. DOI: 10.1021/ja204956b.

(102) Cortizo-Lacalle, D.; Mora-Fuentes, J. P.; Strutyński, K.; Saeki, A.; Melle-Franco, M.; Mateo-Alonso, A. Monodisperse N-Doped Graphene Nanoribbons Reaching 7.7 Nanometers in Length. *Angew. Chem. Int. Ed.* 2018, 57 (3), 703–708. DOI: 10.1002/anie.201710467.

(103) Tran, B. V.; Pham, T. A.; Grunst, M.; Kivala, M.; Stöhr, M. Surface-confined [2 + 2] cycloaddition towards one-dimensional polymers featuring cyclobutadiene units. *Nanoscale* 2017, 9 (46), 18305–18310. DOI: 10.1039/C7NR06187K.

(104) Zhang, L.; Zhang, Y.-Q.; Chen, Z.; Lin, T.; Paszkiewicz, M.; Hellwig, R.; Huang, T.; Ruben, M.; Barth, J. V.; Klappenberger, F. On-Surface Activation of Trimethylsilyl-Terminated Alkynes on Coinage Metal Surfaces. *ChemPhysChem* 2019, 20 (18), 2382–2393. DOI: 10.1002/cphc.201900249.

(105) Kawai, S.; Krejčí, O.; Foster, A. S.; Pawlak, R.; Xu, F.; Peng, L.; Orita, A.; Meyer, E. Diacetylene Linked Anthracene Oligomers Synthesized by One-Shot Homocoupling of Trimethylsilyl on Cu(111). *ACS Nano* 2018, 12 (8), 8791–8797. DOI: 10.1021/acsnano.8b05116.

(106) Zhang, R.; Xia, B.; Xu, H.; Lin, N. Identifying Multinuclear Organometallic Intermediates in On-Surface [2+2] Cycloaddition Reactions. *Angew. Chem. Int. Ed.* 2019, 58 (46), 16485–16489. DOI: 10.1002/anie.201909278.

(107) Sánchez-Sánchez, C.; Dienel, T.; Nicolai, A.; Kharche, N.; Liang, L.; Daniels, C.; Meunier, V.; Liu, J.; Feng, X.; Müllen, K.; Sánchez-Valencia, J. R.; Gröning, O.; Ruffieux, P.; Fasel, R. On-Surface Synthesis and Characterization of Acene-Based Nanoribbons Incorporating Four-Membered Rings. *Chem. Eur. J.* 2019, 25 (52), 12074–12082. DOI: 10.1002/chem.201901410.

(108) Della Pia, A.; Riello, M.; Lawrence, J.; Stassen, D.; Jones, T. S.; Bonifazi, D.; Vita, A. de; Costantini, G. Two-Dimensional Ketone-Driven Metal–Organic Coordination on Cu(111). *Chem. Eur. J.* 2016, 22 (24), 8105–8112. DOI: 10.1002/chem.201600368.

(109) Papageorgiou, A. C.; Li, J.; Oh, S. C.; Zhang, B.; Sağlam, Ö.; Guo, Y.; Reichert, J.; Marco, A. B.; Cortizo-Lacalle, D.; Mateo-Alonso, A.; Barth, J. V. Tuning the ease of

## References

formation of on-surface metal-adatom coordination polymers featuring diketones.

Nanoscale 2018, 10 (20), 9561–9568. DOI: 10.1039/C8NR02537A.

(110) Zhou, H.-C. “.; Kitagawa, S. Metal–Organic Frameworks (MOFs). Chemical Society Reviews 2014, 43 (16), 5415–5418. DOI: 10.1039/C4CS90059F.

(111) Furukawa, H.; Cordova, K. E.; O’Keeffe, M.; Yaghi, O. M. The Chemistry and Applications of Metal-Organic Frameworks. Science 2013, 341 (6149), 1230444. DOI: 10.1126/science.1230444.

(112) Introduction to Metal–Organic Frameworks. Chemical Reviews 2012, 112 (2), 673–674. DOI: 10.1021/cr300014x.

(113) Peng, Y.; Li, Y.; Ban, Y.; Jin, H.; Jiao, W.; Liu, X.; Yang, W. Metal-organic framework nanosheets as building blocks for molecular sieving membranes. Science 2014, 346 (6215), 1356. DOI: 10.1126/science.1254227.

(114) Rodenas, T.; Luz, I.; Prieto, G.; Seoane, B.; Miro, H.; Corma, A.; Kapteijn, F.; Llabrés i Xamena, Francesc X.; Gascon, J. Metal–organic framework nanosheets in polymer composite materials for gas separation. Nat Mater 2015, 14 (1), 48–55. DOI: 10.1038/nmat4113.

(115) Wang, X.; Chi, C.; Zhang, K.; Qian, Y.; Gupta, K. M.; Kang, Z.; Jiang, J.; Zhao, D. Reversed thermo-switchable molecular sieving membranes composed of two-dimensional metal-organic nanosheets for gas separation. Nature Communications 2017, 8 (1), 14460. DOI: 10.1038/ncomms14460.

(116) Zhao, S.; Wang, Y.; Dong, J.; He, C.-T.; Yin, H.; An, P.; Zhao, K.; Zhang, X.; Gao, C.; Zhang, L.; Lv, J.; Wang, J.; Zhang, J.; Khattak, A. M.; Khan, N. A.; Wei, Z.; Zhang, J.; Liu, S.; Zhao, H.; Tang, Z. Ultrathin metal–organic framework nanosheets for electrocatalytic oxygen evolution. Nature Energy 2016, 1 (12), 16184. DOI: 10.1038/nenergy.2016.184.

(117) Cao, L.; Lin, Z.; Peng, F.; Wang, W.; Huang, R.; Wang, C.; Yan, J.; Liang, J.; Zhang, Z.; Zhang, T.; Long, L.; Sun, J.; Lin, W. Self-Supporting Metal–Organic Layers as Single-Site

Solid Catalysts. *Angew. Chem. Int. Ed.* 2016, 55 (16), 4962–4966. DOI: 10.1002/anie.201512054.

(118) Zhao, M.; Wang, Y.; Ma, Q.; Huang, Y.; Zhang, X.; Ping, J.; Zhang, Z.; Lu, Q.; Yu, Y.; Xu, H.; Zhao, Y.; Zhang, H. Ultrathin 2D Metal–Organic Framework Nanosheets. *Adv. Mater.* 2015, 27 (45), 7372–7378. DOI: 10.1002/adma.201503648.

(119) Feng, D.; Lei, T.; Lukatskaya, M. R.; Park, J.; Huang, Z.; Lee, M.; Shaw, L.; Chen, S.; Yakovenko, A. A.; Kulkarni, A.; Xiao, J.; Fredrickson, K.; Tok, J. B.; Zou, X.; Cui, Y.; Bao, Z. Robust and conductive two-dimensional metal–organic frameworks with exceptionally high volumetric and areal capacitance. *Nature Energy* 2018, 3 (1), 30–36. DOI: 10.1038/s41560-017-0044-5.

(120) Sheberla, D.; Bachman, J. C.; Elias, J. S.; Sun, C.-J.; Shao-Horn, Y.; Dincă, M. Conductive MOF electrodes for stable supercapacitors with high areal capacitance. *Nat Mater* 2017, 16 (2), 220–224. DOI: 10.1038/nmat4766.

(121) Campbell, M. G.; Sheberla, D.; Liu, S. F.; Swager, T. M.; Dincă, M. Cu<sub>3</sub>(hexaiminotriphenylene)<sub>2</sub>: An Electrically Conductive 2D Metal–Organic Framework for Chemiresistive Sensing. *Angew. Chem. Int. Ed.* 2015, 54 (14), 4349–4352. DOI: 10.1002/anie.201411854.

(122) Dong, R.; Pfeiffermann, M.; Liang, H.; Zheng, Z.; Zhu, X.; Zhang, J.; Feng, X. Large-Area, Free-Standing, Two-Dimensional Supramolecular Polymer Single-Layer Sheets for Highly Efficient Electrocatalytic Hydrogen Evolution. *Angew. Chem. Int. Ed.* 2015, 54 (41), 12058–12063. DOI: 10.1002/anie.201506048.

(123) Jia, H.; Yao, Y.; Zhao, J.; Gao, Y.; Luo, Z.; Du, P. A novel two-dimensional nickel phthalocyanine-based metal–organic framework for highly efficient water oxidation catalysis. *Journal of Materials Chemistry A* 2018, 6 (3), 1188–1195. DOI: 10.1039/C7TA07978H.

(124) DeGayner, J. A.; Jeon, I.-R.; Sun, L.; Dincă, M.; Harris, T. D. 2D Conductive Iron-Quinoid Magnets Ordering up to T<sub>c</sub> = 105 K via Heterogenous Redox Chemistry. *Journal*

## References

of the American Chemical Society 2017, 139 (11), 4175–4184. DOI: 10.1021/jacs.7b00705.

(125) Tian, Y.; Wang, Y.; Yan, L.; Zhao, J.; Su, Z. Electrochemical reduction of carbon dioxide on the two-dimensional M<sub>3</sub>(Hexaiminotriphenylene)<sub>2</sub> sheet: A computational study. *Applied Surface Science* 2019, 467-468, 98–103. DOI: 10.1016/j.apsusc.2018.10.131.

(126) Dong, R.; Zhang, T.; Feng, X. Interface-Assisted Synthesis of 2D Materials: Trend and Challenges. *Chemical Reviews* 2018, 118 (13), 6189–6235. DOI: 10.1021/acs.chemrev.8b00056.

(127) Maeda, H.; Sakamoto, R.; Nishihara, H. Interfacial synthesis of electrofunctional coordination nanowires and nanosheets of bis(terpyridine) complexes. *Coordination Chemistry Reviews* 2017, 346, 139–149. DOI: 10.1016/j.ccr.2017.02.013.

(128) Zhang, R.; Liu, J.; Gao, Y.; Hua, M.; Xia, B.; Knecht, P.; Papageorgiou, A. C.; Reichert, J.; Barth, J. V.; Xu, H.; Huang, L.; Lin, N. On-surface Synthesis of a Semiconducting 2D Metal–Organic Framework Cu<sub>3</sub>(C<sub>6</sub>O<sub>6</sub>) Exhibiting Dispersive Electronic Bands. *Angew. Chem. Int. Ed.* 2020, 59 (7), 2669–2673. DOI: 10.1002/anie.201913698.

(129) Stepanow, S.; Ohmann, R.; Leroy, F.; Lin, N.; Strunskus, T.; Wöll, C.; Kern, K. Rational Design of Two-Dimensional Nanoscale Networks by Electrostatic Interactions at Surfaces. *ACS Nano* 2010, 4 (4), 1813–1820. DOI: 10.1021/nn100303z.

(130) Seitsonen, A. P.; Lingenfelder, M.; Spillmann, H.; Dmitriev, A.; Stepanow, S.; Lin, N.; Kern, K.; Barth, J. V. Density Functional Theory Analysis of Carboxylate-Bridged Diiron Units in Two-Dimensional Metal–Organic Grids. *Journal of the American Chemical Society* 2006, 128 (17), 5634–5635. DOI: 10.1021/ja060180y.

(131) Urgel, J. I.; Cirera, B.; Wang, Y.; Auwärter, W.; Otero, R.; Gallego, J. M.; Alcamí, M.; Klyatskaya, S.; Ruben, M.; Martín, F.; Miranda, R.; Ecija, D.; Barth, J. V. Surface-Supported Robust 2D Lanthanide-Carboxylate Coordination Networks. *Small* 2015, 11 (47), 6358–6364. DOI: 10.1002/sml.201502761.

- (132) Stepanow, S.; Ohmann, R.; Leroy, F.; Lin, N.; Strunskus, T.; Wöll, C.; Kern, K. Rational Design of Two-Dimensional Nanoscale Networks by Electrostatic Interactions at Surfaces. *ACS Nano* 2010, 4 (4), 1813–1820. DOI: 10.1021/nn100303z.
- (133) Nakada, K.; Fujita, M.; Dresselhaus, G.; Dresselhaus, M. S. Edge state in graphene ribbons: Nanometer size effect and edge shape dependence. *Phys. Rev. B* 1996, 54 (24), 17954–17961. DOI: 10.1103/PhysRevB.54.17954.
- (134) Han, M. Y.; Özyilmaz, B.; Zhang, Y.; Kim, P. Energy Band-Gap Engineering of Graphene Nanoribbons. *Phys. Rev. Lett.* 2007, 98 (20), 206805. DOI: 10.1103/PhysRevLett.98.206805.
- (135) Chen, Z.; Lin, Y.-M.; Rooks, M. J.; Avouris, P. Graphene nano-ribbon electronics. *Physica E: Low-dimensional Systems and Nanostructures* 2007, 40 (2), 228–232. DOI: 10.1016/j.physe.2007.06.020.
- (136) Son, Y.-W.; Cohen, M. L.; Louie, S. G. Energy Gaps in Graphene Nanoribbons. *Phys. Rev. Lett.* 2006, 97 (21), 216803. DOI: 10.1103/PhysRevLett.97.216803.
- (137) G. Liang; N. Neophytou; D. E. Nikonov; M. S. Lundstrom. Performance Projections for Ballistic Graphene Nanoribbon Field-Effect Transistors. *IEEE Transactions on Electron Devices* 2007, 54 (4), 677–682. DOI: 10.1109/TED.2007.891872.
- (138) Wang, X.; Ouyang, Y.; Li, X.; Wang, H.; Guo, J.; Dai, H. Room-Temperature All-Semiconducting Sub-10-nm Graphene Nanoribbon Field-Effect Transistors. *Phys. Rev. Lett.* 2008, 100 (20), 206803. DOI: 10.1103/PhysRevLett.100.206803.
- (139) Hsu, H.; Reichl, L. E. Selection rule for the optical absorption of graphene nanoribbons. *Phys. Rev. B* 2007, 76 (4), 45418. DOI: 10.1103/PhysRevB.76.045418.
- (140) Guo, J.; Gunlycke, D.; White, C. T. Field effect on spin-polarized transport in graphene nanoribbons. *Applied Physics Letters* 2008, 92 (16), 163109. DOI: 10.1063/1.2908207.
- (141) Son, Y.-W.; Cohen, M. L.; Louie, S. G. Half-metallic graphene nanoribbons. *Nature* 2006, 444 (7117), 347–349. DOI: 10.1038/nature05180.

## References

- (142) Li, X.; Wang, X.; Zhang, L.; Lee, S.; Dai, H. Chemically Derived, Ultrasoft Graphene Nanoribbon Semiconductors. *Science* 2008, 319 (5867), 1229. DOI: 10.1126/science.1150878.
- (143) Barone, V.; Hod, O.; Scuseria, G. E. Electronic Structure and Stability of Semiconducting Graphene Nanoribbons. *Nano Letters* 2006, 6 (12), 2748–2754. DOI: 10.1021/nl0617033.
- (144) Yang, L.; Park, C.-H.; Son, Y.-W.; Cohen, M. L.; Louie, S. G. Quasiparticle Energies and Band Gaps in Graphene Nanoribbons. *Phys. Rev. Lett.* 2007, 99 (18), 186801. DOI: 10.1103/PhysRevLett.99.186801.
- (145) Campos-Delgado, J.; Romo-Herrera, J. M.; Jia, X.; Cullen, D. A.; Muramatsu, H.; Kim, Y. A.; Hayashi, T.; Ren, Z.; Smith, D. J.; Okuno, Y.; Ohba, T.; Kanoh, H.; Kaneko, K.; Endo, M.; Terrones, H.; Dresselhaus, M. S.; Terrones, M. Bulk Production of a New Form of sp<sup>2</sup> Carbon: Crystalline Graphene Nanoribbons. *Nano Letters* 2008, 8 (9), 2773–2778. DOI: 10.1021/nl801316d.
- (146) Bai, J.; Duan, X.; Huang, Y. Rational Fabrication of Graphene Nanoribbons Using a Nanowire Etch Mask. *Nano Letters* 2009, 9 (5), 2083–2087. DOI: 10.1021/nl900531n.
- (147) Jiao, L.; Zhang, L.; Wang, X.; Diankov, G.; Dai, H. Narrow graphene nanoribbons from carbon nanotubes. *Nature* 2009, 458 (7240), 877–880. DOI: 10.1038/nature07919.
- (148) Hu, Y.; Xie, P.; Corato, M. de; Ruini, A.; Zhao, S.; Meggendorfer, F.; Straasø, L. A.; Rondin, L.; Simon, P.; Li, J.; Finley, J. J.; Hansen, M. R.; Lauret, J.-S.; Molinari, E.; Feng, X.; Barth, J. V.; Palma, C.-A.; Prezzi, D.; Müllen, K.; Narita, A. Bandgap Engineering of Graphene Nanoribbons by Control over Structural Distortion. *Journal of the American Chemical Society* 2018, 140 (25), 7803–7809. DOI: 10.1021/jacs.8b02209.